Hindawi
Mathematical Problems in Engineering
Volume 2018, Article ID 7159891, 22 pages
https://doi.org/10.1155/2018/7159891

Research Article

A Novel Sliding Mode Control Framework for Electrohydrostatic Position Actuation System

Rongrong Yang[1], **Yongling Fu**[1], **Ling Zhang**[1], **Haitao Qi**[2], **Xu Han**[1] and **Jian Fu**[1]

[1] *School of Mechanical Engineering and Automation, Beihang University, Beijing 100191, China*
[2] *Engineering Training Center, Beihang University, Beijing 100191, China*

Correspondence should be addressed to Haitao Qi; qhtbuaa@163.com

Received 22 May 2017; Accepted 18 December 2017; Published 17 January 2018

Academic Editor: Hung-Yuan Chung

A novel sliding mode control (SMC) design framework is devoted to providing a favorable SMC design solution for the position tracking control of electrohydrostatic actuation system (EHSAS). This framework is composed of three submodules as follows: a reduced-order model of EHSAS, a disturbance sliding mode observer (DSMO), and a new adaptive reaching law (NARL). First, a reduced-order model is obtained by analyzing the flow rate continuation equation of EHSAS to avoid the use of a state observer. Second, DSMO is proposed to estimate and compensate mismatched disturbances existing in the reduced-order model. In addition, a NARL is developed to tackle the inherent chattering problem of SMC. Extensive simulations are conducted compared with the wide adoption of three-loop PID method on the cosimulation platform of EHSAS, which is built by combining AMESim with MATLAB/Simulink, to verify the feasibility and superiority of the proposed scheme. Results demonstrate that the chattering can be effectively attenuated, and the mismatched disturbance can be satisfyingly compensated. Moreover, the transient performance, steady-state accuracy, and robustness of position control are all improved.

1. Introduction

Electrohydrostatic actuation system (EHSAS) is a typical self-contained electrohydraulic servo system. EHSAS does not require an extra external hydraulic oil source compared with the traditional valve-controlled electrohydraulic servo system (VEHAS), and control of position, velocity, and output force of EHSAS is implemented by regulating the speed of motor pump instead of the throttling principle of VEHAS. In contrast to electrical counterpart, that is, an electromechanical actuation system (EMAS), EHSAS has the higher power-to-weight ratio and no mechanical jam fault. Thus, EHSAS demonstrates many advantages, such as high efficiency, high reliability, compact structure, and stable output force. EHSAS has been applied in a variety of fields, such as more electric actuation system of aircraft or ship [1, 2], active suspension of a vehicle [3, 4], angle control of cannon and radar, flow rate and pressure control of injection molding machine [5–7], and position and force control of robot [8–11]. Moreover, the superiority of EHSAS has become prominent with the recent emergence of several new components, such as an integrated electrohydraulic pump (IEHP) and single-rod symmetrical cylinder. In the future, improved control accuracy, higher frequency bandwidth, and stronger robustness will be the development trends of EHSAS. However, achieving these performances, which can be attributed to the following reasons, is a challenging task. First, EHSAS includes numerous uncertain parameters, such as oil-effective bulk modulus, leakage coefficient, and load mass given the influence of oil temperature, sealing, and different operating conditions. Second, the dynamic characteristics of friction and external load disturbance are difficult to exactly acquire, which have an adverse impact on control performance.

In addition, EHSAS typically adopts permanent magnet synchronous motor (PMSM) as the drive motor of the pump to increase the power-to-weight ratio. However, PMSM is nonlinear, multivariable and strong coupling objective such that the control of motor is more complex than that of servo

valve in VEHAS. Furthermore, if the IEHP is used in EHSAS, because the motor is integrated into the internal part of the pump, which places the motor in a fully fresh circumstance, then the uncertainties will be more complicated.

Thus far, various control methods have been proposed to address these problems for improving the performance of EHSAS. Among these schemes, the control structure of three loops (i.e., position, motor pump speed, and current control loops) based on PID is dominated in practice because of its simplicity. In [12, 13], fuzzy method and structure invariance principle were used to tune the PI parameters of the three loops and compensate external disturbance. However, fuzzy rules typically depend on specialists to a large extent, thus resulting in poor adaptability in practice. In [14], a multiloop control approach was addressed by using high gain to dominate uncertainties, which result in oscillation and even instability due to light damping feature of EHSAS. In addition, other control schemes, such as quantitative feedback theory [15, 16], model reference adaptive [17], and $H\infty$ [18], have been developed to strengthen robustness. Moreover, many nonlinear strategies were investigated to further enhance the performance of EHSAS. Literature [19] utilizes feedback linearization to cancel nonlinear functions in a system. In [20, 21], adaptive backstepping with a neural network was presented to estimate uncertainties and guarantee asymptotic stability of a system, but this method requires that all system state variables were measurable, and the neural network was excessively complex to apply in practice. In [22], a passive-based model was introduced in which state and disturbance observers were adopted to observe unmeasured state and unknown disturbance.

Sliding mode control (SMC) is a powerful robust control strategy for the linear or nonlinear system due to its insensibility to uncertainties and laconic design procedure. However, three main problems, that is, (1) obtaining full system state information, (2) coping with mismatched disturbances, and (3) inherent chattering problem, should be addressed when using SMC because EHSAS is a high-order nonlinear system subjected to multiple mismatched disturbances. The first problem is commonly solved by state observer [23, 24], but the observed states cannot converge to its actual value if nonvanishing mismatched disturbance exists in the system, thereby resulting in a complicated design process. To the best of our knowledge, nearly all existing literature handles the second problem by transforming mismatched to matched disturbance [25–30]. This solution will result in undesirable consequences in which several originally measurable states cannot be utilized; instead, new unmeasurable states will be generated such that an additional state observer is required. For the last problem, abundant approaches, such as boundary layer method [31], high-order SMC [32], and adaptive SMC [33], have been explored to mitigate or eliminate chattering. In addition, the aforementioned literature that uses SMC for EHSAS ignores the control of motor pump for its fast dynamic behavior. Actually, the speed and current control dynamic performances of the motor pump have a significant effect on the position control performance of EHSAS.

In this paper, first, a simplified model is presented by considering leakage and oil compression flow rate as a lumped disturbance; then, mechanical and hydraulic subsystems and motor pump are regarded as a whole for SMC design in which the voltage control signal of the motor pump is obtained directly. State observers are unnecessary to design after simplification because the system states used are all measurable. Second, a finite time disturbance sliding mode observer (DSMO) is designed to estimate the mismatched disturbance and its derivative that are integrated into a sliding mode surface to guarantee the asymptotic convergence of position tracking error. In addition, a kind of new adaptive reaching law (NARL), which not only ensures faster reaching speed but also achieves an improved chattering attenuation effect, is presented.

The remainder of this paper is organized as follows. In Section 2, the configuration of the EHSAS and basic principle of the IEHP are introduced, and the full-order and simplified model of EHSAS are presented. In Section 3, the detained design of procedure of DSMO and its stability analysis are discussed. In Section 4, the position and d-axis current sliding mode controller of the EHSAS are designed. In Section 5, a kind of NARL is proposed, and comparative analyses with other reaching laws are conducted. In Section 6, simulation results and analysis are given. In Section 7, conclusions are drawn.

2. System Description and Model Simplification

2.1. EHSAS Description. The hydraulic schematic of EHSAS is depicted in Figure 1. EHSAS consists of a bidirectional IEHP, symmetrical hydraulic cylinder, an accumulator, check valve, relief valve, mode selector valve, sensors, controller, power driver of an IEHP, and other accessories. Among these components, the IEHP is a new hydraulic power unit that is highly integrated with PMSM and axial piston pump, and its structure diagram is illustrated in Figure 2 [34, 35]. The basic operational principle is introduced as follows: DC270V voltage is connected by a power connector and is transformed into a sinusoidal AC voltage by an inverter that is utilized to generate a rotating magnetic field. The rotating magnetic field interacts with a permanent magnet of rotor surface to drive rotor rotation. Consequently, the oil suction and discharge processes are achieved through piston motion coordination with swash and valve plates. A resolver is used to detect rotor magnet pole position and measure the speed of IEHP. The structure of which is highly different, although the working principle of the IEHP is the same as that of the traditional motor pump unit. The IEHP has high efficiency, small size, and minimal noise because motor and pump share the same rotor and housing instead of the link form by couplings used in the traditional motor pump. Oil will be compressed to cause load motion by regulating the speed of the IEHP to generate flow rate. An accumulator is responsible for supplying oil to low-pressure pipe by check valve to prevent cavitation. Two relief valves are used to restrict the maximum operation pressure of the EHSAS for safety. Mode switch valve is installed to keep the piston in a free state when a fault occurs.

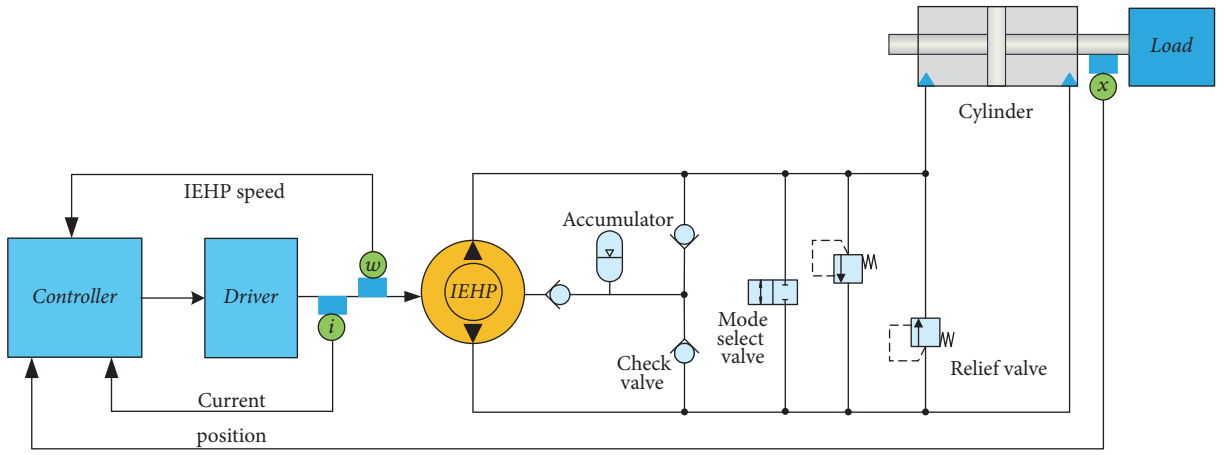

Figure 1: Hydraulic diagram of the EHSAS.

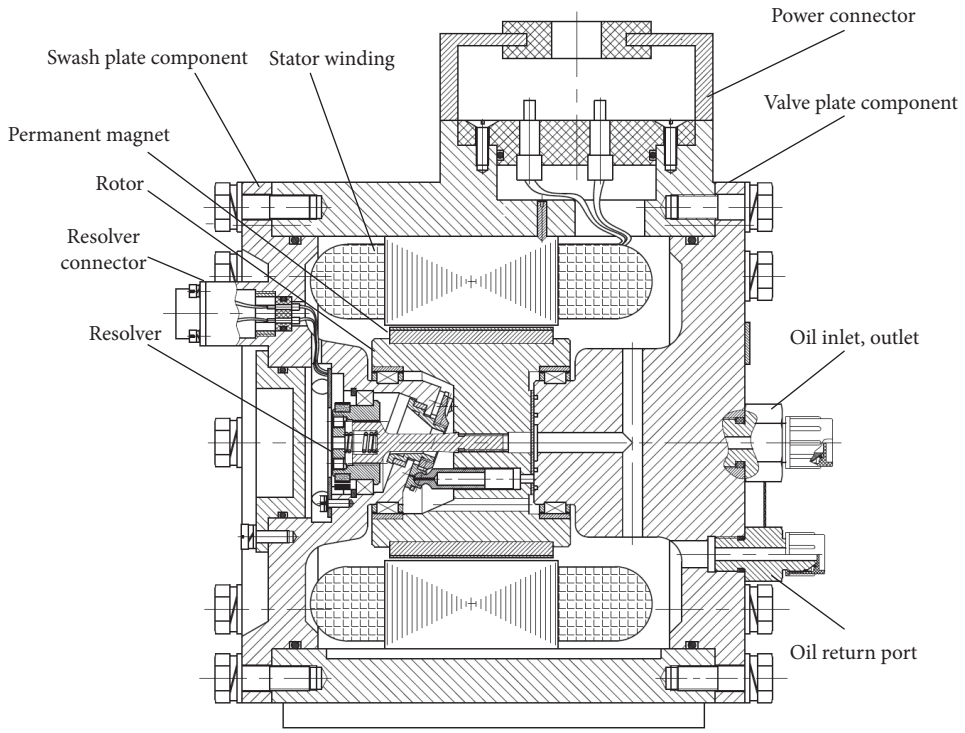

Figure 2: Structural diagram of the IEHP.

2.2. Mathematical Model and Simplification. The shape of magnetic flux density remains nearly sinusoidal, although an oil gap instead of gas gap exists between the stator and the rotor of the IEHP. Thus, the voltage equations of the d- and q-axes of the IEHP can be expressed as

$$u_d = L_d \dot{i}_d + R i_d - p\omega_m L_q i_q, \tag{1}$$

$$u_q = L_q \dot{i}_q + R i_q + p\omega_m L_d i_d + p\omega_m \psi_f. \tag{2}$$

The electromagnetic torque T_e of the IEHP is described by

$$T_e = 1.5 p i_q \left[\psi_f + i_d \left(L_d - L_q\right)\right], \tag{3}$$

where u_d and u_q are the voltages of the d- and q-axes, respectively, i_d and i_q represent the currents of the d- and q-axes, correspondingly, L_d and L_q are the equivalent inductances of the d- and q-axes, respectively, R is the resistance of stator winding, p is the number of pole pairs, ψ_f represents the magnet flux of the rotor permanent magnet, and ω_m is the mechanical angular speed.

The oil gap friction between the stator and the rotor can be described as [36]

$$T_{L1} = \frac{2\pi\mu L r^3 \omega_m}{\kappa} = b_2 \omega_m. \tag{4}$$

The motion equation of the IEHP is expressed as

$$J_t\dot{\omega}_m = T_e - DP_L - B_m\omega_m - T_f, \tag{5}$$

where μ is the oil kinetic viscosity, L is the length of the rotor, r is the radius of the rotor, κ represents the thickness of the oil gap between the rotor and the stator, T_f is the other unmodeled nonlinear friction and disturbance, J_t is the moment of inertia of the IEHP, b_1 is the mechanical viscous friction coefficient, b_2 is the oil gap viscous friction coefficient, $B_m = b_1 + b_2$ is the total viscous friction coefficient, D represents the volumetric displacement of the IEHP, and P_L is the pressure difference of the two chambers of the cylinder.

The flow rate equation of the two champers of the IEHP can be defined as

$$\begin{aligned} Q_a &= D\omega_m - \varepsilon\left(p_a - p_b\right) - L_1\left(p_a - p_r\right) - \frac{V_a}{\beta_e}\dot{p}_a, \\ Q_b &= D\omega_m - \varepsilon\left(p_a - p_b\right) + L_1\left(p_a - p_r\right) + \frac{V_b}{\beta_e}\dot{p}_b, \end{aligned} \tag{6}$$

where ε and L_1 are the internal and external leakage coefficients of the IEHP, respectively, Q_a and Q_b represent the inlet and outlet flow rates of the IEHP, correspondingly, p_a and p_b are the pressures of the two chambers of the IEHP, respectively, V_a and V_b are the volumes of the two chambers of the IEHP, and β_e is the effective oil bulk modulus.

For the cylinder, the flow rate equation can be expressed by

$$\begin{aligned} Q_1 &= A\dot{x} + \frac{V_0 + Ax}{\beta_e}\dot{p}_1 + L_2\left(p_1 - p_2\right), \\ Q_2 &= A\dot{x} - \frac{V_0 - Ax}{\beta_e}\dot{p}_2 + L_2\left(p_1 - p_2\right), \end{aligned} \tag{7}$$

where L_2 is the internal leakage coefficient of the cylinder, and the external leakage is ignored, Q_1 and Q_2 represent the supplied and return flow rates of the cylinder, correspondingly, p_1 and p_2 are the pressures of the two champers of the cylinder, respectively, V_0 is the initial volume of the single chamber of the cylinder, A is the effective ram area of the cylinder, and x represents the displacement of the load.

The following equation can be obtained according to flow rate continuity principle:

$$\begin{aligned} Q_1 &= Q_a, \\ Q_2 &= Q_b. \end{aligned} \tag{8}$$

The following relationships are also considered:

$$\begin{aligned} \dot{p}_1 &= \dot{p}_a, \\ \dot{p}_2 &= \dot{p}_b, \\ \dot{p}_1 &= -\dot{p}_2. \end{aligned} \tag{9}$$

The simplified flow rate continuity equation can be acquired by combining (7)–(9), as follows:

$$\begin{aligned} D\omega_m &= A\dot{x} + \frac{V_0 + V_a}{2\beta_e}\dot{p}_L + \left(\varepsilon + L_2 + \frac{L_1}{2}\right)p_L \\ &= A\dot{x} + \frac{V_t}{4\beta_e}\dot{p}_L + C_t p_L + Q_f, \end{aligned} \tag{10}$$

where V_t is the total control volume and Q_f is the flow rate consumption of all kinds of valves in the EHSAS.

The load is assumed to be rigidly linked with rod, then the motion equation of load can be written as

$$Ap_L = M\ddot{x} + K_s x + B_c\dot{x} + F_f + F_L, \tag{11}$$

where $M = m_L + m_c$, M denotes the combined mass, including piston, rod, and load, m_c is the mass of piston and rod, m_L is the mass of load, K_s is the stiffness coefficient of the elastic load, F_L is the external load force, B_c is the viscous friction coefficient, and F_f is the other unmodeled nonlinear friction and disturbance.

The system state vector is defined as

$$\begin{aligned} \mathbf{X} &= \begin{bmatrix} x_1 & x_2 & x_3 & x_4 & x_5 & x_6 \end{bmatrix}^T \\ &= \begin{bmatrix} x & \dot{x} & p_L & \omega_m & i_q & i_d \end{bmatrix}^T. \end{aligned} \tag{12}$$

Then, the state equations of the EHSAS can be denoted as

$$\begin{aligned} \dot{x}_1 &= x_2, \\ \dot{x}_2 &= \frac{A}{M}x_3 - \frac{K_s}{M}x_1 - \frac{B_m}{M}x_2 - \frac{F_f}{M} - \frac{F_L}{M}, \\ \dot{x}_3 &= -\frac{4\beta_e A}{V_t}x_2 - \frac{4\beta_e C_t}{V_t}x_3 + \frac{4\beta_e D}{V_t}x_4, \\ \dot{x}_4 &= \frac{1.5px_5}{J_t}\left[\psi_f + x_6\left(L_d - L_q\right)\right] - \frac{B_m}{J_t}x_2 - \frac{D}{J_t}x_3 \\ &\quad - \frac{T_f}{J_t}, \\ \dot{x}_5 &= -\frac{pL_d}{L_q}x_4x_6 - \frac{p\psi_f}{L_q}x_4 - \frac{R}{L_q}x_5 + \frac{u_q}{L_q}, \\ \dot{x}_6 &= \frac{pL_q}{L_d}x_4x_5 - \frac{R}{L_d}x_6 + \frac{u_d}{L_d}. \end{aligned} \tag{13}$$

In (13), the EHSAS is composed of a fifth- and a first-order subsystem, and u_q and u_d are the corresponding control inputs of the two subsystems. Our control objective is to synthesize control voltage u_q for displacement x to track the desired position x_d as accurately as possible in the presence of parametric variations and external disturbance.

According to the principle of EHSAS, the corresponding velocity $\dot{x}$ and acceleration $\ddot{x}$ are necessary to accomplish the control task of displacement x. Velocity $\dot{x}$ is generated by flow rate that results from the speed adjustment of the IEHP, and acceleration $\ddot{x}$ is derived from pressure p_L for the

compression of oil, thereby also resulting from the flow rate of the IEHP. Therefore, the control of position is equivalent to regulating the speed ω_m of the IEHP in essence. In (10), the total output flow rate of the IEHP includes three parts as follows: the first term $A\dot{x}$ represents the demanded flow rate of load movement; the second term $(V_t/4\beta_e)\dot{p}_L$ is the flow rate consumption due to oil compression; and the last two terms $C_t p_L$ and Q_f are the leakage flow rate and consumption of various valves, respectively. In general, the first part represents a large proportion of the total flow rate; then, the fifth-order subsystem will be reduced to third order if the other two parts are considered as a lumped disturbance.

The system state vector is redefined as

$$\mathbf{Z} = \begin{bmatrix} z_1 & z_2 & z_3 & z_4 \end{bmatrix}^T = \begin{bmatrix} x & \omega_m & i_q & i_d \end{bmatrix}^T. \tag{14}$$

The system state equations are rewritten by

$$\begin{aligned} \dot{z}_1 &= a_1 z_2 + d_1, \\ \dot{z}_2 &= a_2 z_3 + a_3 z_3 z_4 + d_2, \\ \dot{z}_3 &= a_5 z_2 z_4 + a_6 z_2 + a_7 z_3 + b_1 u_q, \\ \dot{z}_4 &= a_8 z_2 z_3 + a_9 z_4 + b_2 u_d, \end{aligned} \tag{15}$$

where

$$\begin{aligned} a_1 &= \frac{D}{A}, \\ d_1 &= -\frac{1}{A}\left(\frac{V_t}{4\beta_e}\frac{dp_L}{dt} + C_t p_L + Q_f\right), \\ a_2 &= \frac{1.5p\psi_f}{J_t}, \\ a_3 &= \frac{1.5p}{J_t}\left(L_d - L_q\right), \\ d_2 &= -\frac{B_m}{J_t}z_2 - \frac{D}{J_t}p_L - \frac{1}{J_t}F_f, \\ a_5 &= -\frac{pL_d}{L_q}, \\ a_6 &= -\frac{p\psi_f}{L_q}, \\ a_7 &= -\frac{R}{L_q}, \\ b_1 &= \frac{1}{L_q}, \\ a_8 &= \frac{pL_q}{L_d}, \\ a_9 &= -\frac{R}{L_d}, \\ b_2 &= \frac{1}{L_d}. \end{aligned} \tag{16}$$

The IEHP adopts vector control with the form of $i_d = 0$, and system state variables are reselected for ease of description as

$$\mathbf{\Psi} = \begin{bmatrix} \psi_1 & \psi_2 & \psi_3 & z_4 \end{bmatrix}^T = \begin{bmatrix} z_1 & a_1 z_2 & a_1 a_2 z_3 & z_4 \end{bmatrix}^T. \tag{17}$$

Then, the simplified state equations can be formulated as

$$\begin{aligned} \dot{\psi}_1 &= \psi_2 + d_1, \\ \dot{\psi}_2 &= \psi_3 + a_1 d_2, \\ \dot{\psi}_3 &= a_2 a_6 \psi_2 + a_7 \psi_3 + a_1 a_2 b_1 u_q, \\ \dot{z}_4 &= a_8 z_2 z_3 + a_9 z_4 + b_2 u_d. \end{aligned} \tag{18}$$

Remark 1. (1) If pressure sensors are assembled in the two champers of the cylinder, then d_1 and d_2 are calculated partly and can be used for feedforward compensation. However, the pressure signal is easily perturbed by noise owing to its high-frequency bandwidth. Moreover, d_1 includes the derivative of p_L, which results in a severe noise contamination problem. In addition, pressure sensors may not be used because of cost limitations, size, and installation room. (2) Fortunately, the position x of load and the speed ω_m of the IEHP are typically measured by several digital sensors, such as grating scale, encoder, and resolver. Therefore, if these clean signals are employed to design an observer to estimate d_1 and d_2, then the satisfied disturbance compensation effect can be achieved. Based on the above analysis, p_L is unmeasurable, while x, ω_m, i_q, and i_d are all available.

3. Design of a Novel DSMO

3.1. Problem Statement. In (18), d_1, d_2, and u_q are placed in different channels; thus, the simplified third-order system remains a typical perturbed system with mismatched disturbance. The traditional SMC is robust only for matched disturbance, which can be interpreted by the following analysis.

The desired position signal is assumed to satisfy $x_d \in C^3$, and tracking error variables are defined as

$$\begin{aligned} e_1 &= \psi_1 - x_d, \\ e_2 &= \psi_2 - \dot{x}_d, \\ e_3 &= \psi_3 - \ddot{x}_d. \end{aligned} \tag{19}$$

Then, the error dynamic equations can be obtained as

$$\begin{aligned} \dot{e}_1 &= \dot{\psi}_1 - \dot{x}_d = \psi_2 - \dot{x}_d + d_1 = e_2 + d_1, \\ \dot{e}_2 &= \dot{\psi}_2 - \ddot{x}_d = \psi_3 - \ddot{x}_d + a_1 d_2 = e_3 + a_1 d_2, \\ \dot{e}_3 &= \dot{\psi}_3 - \dddot{x}_d = a_2 a_6 \psi_2 + a_7 \psi_3 + a_1 a_2 b_1 u_q - \dddot{x}_d. \end{aligned} \tag{20}$$

The sliding mode variable is selected as $s = e_3 + c_2 e_2 + c_1 e_1$, where c_1 and c_2 meet Hurwitz condition.

Taking the derivative of s with respect to time and considering (20) yield

$$\begin{aligned}\dot{s} &= \dot{e}_3 + c_2\dot{e}_2 + c_1\dot{e}_1 \\ &= a_2a_6\psi_2 + a_7\psi_3 + a_1a_2b_1u_q - \ddot{x}_d + c_2\left(e_3 + a_1d_2\right) \\ &\quad + c_1\left(e_2 + d_1\right).\end{aligned} \tag{21}$$

The constant rate reaching law (CRRL) is used; that is, $\dot{s} = -\eta\,\mathrm{sgn}(s)$. Then, control law u_q can be obtained as

$$\begin{aligned}u_q &= -\left(a_1a_2b_1\right)^{-1} \\ &\quad \cdot \left(a_2a_6\psi_2 + a_7\psi_3 - \ddot{x}_d + c_2e_3 + c_1e_2 + \eta\,\mathrm{sgn}\left(s\right)\right),\end{aligned} \tag{22}$$

where $\eta > 0$ is the switch gain.

The Lyapunov function is defined as $V = 0.5s^2$, and the derivative of V is obtained. Then, substituting (22) into it yields

$$\begin{aligned}\dot{V} &= s\dot{s} = s\left(-\eta\,\mathrm{sgn}\left(s\right) + c_1d_1 + c_2a_1d_2\right) \\ &= -\eta\left|s\right| + s\left(c_3d_1 + c_2a_1d_2\right) \\ &\le -\eta\left|s\right| + \left|s\right|\left(c_3D_1 + c_2a_1D_2\right) \\ &= \left|s\right|\left[\left(c_3D_1 + c_2a_1D_2\right) - \eta\right].\end{aligned} \tag{23}$$

Evidently, $\dot{V} < 0$ can be guaranteed if switch gain η satisfies condition $\eta > c_3D_1 + c_2D_2$. After s reaches sliding mode surface $s = 0$, and noting (20), we obtain

$$\begin{aligned}e_3 + c_2e_2 + c_1e_1 &= \dot{e}_2 - a_1d_2 + c_2\left(\dot{e}_1 - d_1\right) + c_1e_1 \\ &= \ddot{e}_1 + c_2\dot{e}_1 + c_1e_1 - c_2d_1 - \dot{d}_1 - a_1d_2 \\ &= 0.\end{aligned} \tag{24}$$

By simplifying (24), the system dynamic performance is decided by the following equation:

$$\ddot{e}_1 + c_2\dot{e}_1 + c_1e_1 = c_2d_1 + \dot{d}_1 + a_1d_2. \tag{25}$$

In (25), position tracking error e_1 cannot converge asymptotically to 0 given the existence of existing of $d_1, \dot{d}_1$, and d_2. Fortunately, the asymptotic convergence of e_1 can be achieved if a new sliding mode variable σ is designed as

$$\sigma = e_3 + c_2e_2 + c_1e_1 + c_2d_1 + \dot{d}_1 + a_1d_2. \tag{26}$$

However, $d_1, \dot{d}_1$, and d_2 are unknown; thus, a disturbance observer is required to estimate $d_1, \dot{d}_1$, and d_2, which will be presented in the next section.

3.2. Design of the DSMO. In this section, a new DSMO is presented to estimate $d_1, \dot{d}_1$, and d_2. Generally, the design procedure of observer includes two steps. First, the dynamic equations of the system are copied. Second, some correction terms are added to the dynamic equations of the system. In general, these correction terms are a function of the error of measurable output variable and its observation value, which can ensure unmeasurable state variable convergence to its real value. The simplified model in (18) is rewritten as the following form based on the design idea of the observer:

$$\begin{aligned}\dot{\psi}_1 &= \psi_2 + d_1, \\ \dot{d}_1 &= \dot{d}_1, \\ \ddot{d}_1 &= \ddot{d}_1,\end{aligned} \tag{27}$$

$$\begin{aligned}\dot{\psi}_2 &= \psi_3 + a_1d_2, \\ \dot{d}_2 &= \dot{d}_2.\end{aligned} \tag{28}$$

Owing to (14) and (17), the following relationships for ψ_1, ψ_2, and ψ_3 are considered: $\psi_1 = z_1 = x$, $\psi_2 = a_1z_2 = a_1\omega = (D/A)\omega$, and $\psi_3 = a_1a_2z_3 = (D/A)(1.5p\psi_f/J_t)i_q$, where x, ω, and i_q are all measurable, and parameters a_1 and a_2 can also be acquired by using the mechanical, hydraulic, and electrical design parameters of the EHSAS. The difference between approximate and actual values can be seen as a parametric uncertainty lumped into d_1 and d_2, even though the obtained values of a_1 and a_2 are inaccurate. Therefore, we can claim that a_1 and a_2 are known, thereby implying that ψ_1, ψ_2, and ψ_3 are also known. Then, ψ_1 and ψ_2 in (27) are considered measurable output and input variables for estimating d_1 and $\dot{d}_1$. Similarly, ψ_2 and ψ_3 in (28) are regarded as measurable output and input variables that are used to observe d_2.

In addition, the dynamic behavior of d_1, $\dot{d}_1$, $\ddot{d}_1$, and d_2 is required when designing an observer that is impossible to be acquired in practice. Thus, a prevailing method in the existing literature is to assume that d_1, $\dot{d}_1$, $\ddot{d}_1$, and d_2 are bounded. Actually, in (27) and (28), $d_1, \dot{d}_1, \ddot{d}_1$, and d_2 depend on the velocity $\dot{x}$, acceleration $\ddot{x}$, jerk $\dddot{x}$, and acceleration $\ddot{\omega}$ of the IEHP, respectively, and these variables are related to the speed ω of the IEHP, maximum operation pressure $P_{s\max}$ of the EHSAS, maximum output torque $T_{e\max}$ of the IEHP, viscosity μ and bulk modulus β_e of fluid oil, and enclosed volume V_t of the EHSAS. The above-mentioned variables are all constrained. Hence, the bounded assumption about $d_1, \dot{d}_1$, $\ddot{d}_1$, and d_2 is reasonable. Thus, the following assumption is presented.

Assumption 2. $d_1 \in C^2$, $d_2 \in C^1$; moreover, $|d_1| \le D_1$, $|\dot{d}_1| \le D_{1d}$, $|\ddot{d}_1| \le D_{1dd}$, $|d_2| \le D_2$, and $|\dot{d}_2| \le D_{2d}$, where D_1, D_{1d}, D_{1dd}, D_2, and D_{2d} are known constants.

According to the aforementioned analysis, the disturbance observers can be designed as

$$\begin{aligned}\dot{\hat{\psi}}_1 &= \psi_2 + \hat{d}_1 + \mu_1, \\ \dot{\hat{d}}_1 &= \mu_2 + \hat{d}_{1d}, \\ \dot{\hat{d}}_{1d} &= \mu_3,\end{aligned} \tag{29}$$

$$\begin{aligned}\dot{\hat{\psi}}_2 &= \psi_3 + a_1\hat{d}_2 + \mu_4, \\ \dot{\hat{d}}_2 &= \mu_5,\end{aligned}$$

where $\widehat{\psi}_1$, $\widehat{\psi}_2$, $\widehat{d}_1$, $\widehat{d}_{1d}$, and $\widehat{d}_2$ denote the observed values of ψ_1, ψ_2, d_1, $\dot{d}_1$, and d_2, respectively, and μ_1, μ_2, μ_3, μ_4, and μ_5 are the auxiliary correction terms.

Equation (18) is subtracted from (29), then, the error dynamic equations of the observer can be obtained by

$$\begin{aligned}
\dot{\widetilde{\psi}}_1 &= \widetilde{d}_1 - \mu_1,\\
\dot{\widetilde{d}}_1 &= \dot{d}_1 - \mu_2 + \widetilde{d}_{1d},\\
\dot{\widetilde{d}}_{1d} &= \ddot{d}_1 - \mu_3,\\
\dot{\widetilde{\psi}}_2 &= a_1\widetilde{d}_2 - \mu_4,\\
\dot{\widetilde{d}}_2 &= \dot{d}_2 - \mu_5,
\end{aligned} \tag{30}$$

where $\widetilde{\psi}_1$, $\widetilde{\psi}_2$, $\widetilde{d}_1$, $\widetilde{d}_{1d}$, and $\widetilde{d}_2$ represent the observer errors of ψ_1, ψ_2, d_1, $\dot{d}_1$, and d_2, correspondingly.

The detailed design procedures are given in the following.

Step 1. Selecting a sliding mode variable $s_1 = \widetilde{\psi}_1$ and taking derivative of s_1 yields

$$\dot{s}_1 = \dot{\widetilde{\psi}}_1 = \widetilde{d}_1 - \mu_1. \tag{31}$$

Apparently, if appropriate variable μ_1 is designed such that $\dot{\widetilde{\psi}}_1 = 0$, then $\widetilde{d}_1$ will be equal to μ_1. Here, μ_1 is constructed as

$$\mu_1 = \xi_1 s_1 + \xi_2 |s_1|^{0.5} \operatorname{sgn}(s_1) + \eta_1 \operatorname{sgn}(s_1). \tag{32}$$

Defining the Lyapunov function $V_1 = 0.5s_1^2$, differentiating V_1, and substituting (32) into it yield

$$\begin{aligned}
\dot{V}_1 = s_1\dot{s}_1 &= -\xi_1 s_1^2 - \xi_2 |s_1|^{1.5} - \eta_1 |s_1| + s_1\widetilde{d}_1\\
&\le -\eta_1 |s_1| + |s_1|\widetilde{d}_1 = -\sqrt{2}V_1^{0.5}\left(\eta_1 - \widetilde{d}_1\right),
\end{aligned} \tag{33}$$

where ξ_1, ξ_2, and η_1 are all positive constants. Evidently, s_1 will reach a sliding mode surface $s_1 = 0$ in finite time t_1 only if η_1 meets condition $\eta_1 > |\widetilde{d}_1|$.

According to the equivalent control principle of the SMC, $s_1 = \dot{s}_1 = 0$ will hold once sliding mode surface $s_1 = 0$ is reached, and $s_1 = \widetilde{\psi}_1$ is considered. Therefore, $\widetilde{d}_1$ will approach μ_1 in finite time t_1.

Step 2. Based on the acquired $\widetilde{d}_1$ in Step 1, a new sliding mode variable $s_2 = \widetilde{d}_1$ is selected, and μ_2 is designed as the following form:

$$\mu_2 = \xi_3 s_2 + \xi_4 |s_2|^{0.5} \operatorname{sgn}(s_2) + \eta_2 \operatorname{sgn}(s_2), \tag{34}$$

where ξ_3, ξ_4, and η_2 are all positive constants.

If η_2 is selected to meet the condition $\eta_2 > |D_{1d} + \widetilde{d}_{1d}|$, then $\widetilde{d}_1$ and s_2 will converge to 0 in finite time t_2 after undergoing finite time t_1, thereby also indicating that $\widehat{d}_1$ converges to d_1 at in finite time t_2. Thus, $\widetilde{d}_{1d}$ will also approach μ_2 in finite time t_2 based on equivalent control principle.

Step 3. Continuing selecting sliding mode variable $s_3 = \widetilde{d}_{1d}$, then μ_3 is constructed as

$$\mu_3 = \xi_5 s_3 + \xi_6 |s_3|^{0.5} \operatorname{sgn}(s_3) + \eta_3 \operatorname{sgn}(s_3), \tag{35}$$

where ξ_5, ξ_6, and η_3 are all positive constants.

If η_3 is selected to satisfy $\eta_3 > D_{1dd}$, then $\widetilde{d}_{1d}$ and s_3 can converge to 0 in finite time t_3 after undergoing finite time $t_1 + t_2$, thereby indicating that $\widehat{d}_{1d}$ converges to $\dot{d}_1$ in finite time t_3.

Step 4. Two sliding variables $s_4 = \widetilde{\psi}_2$ and $s_5 = \widetilde{d}_2$ are selected; similarly, μ_4 and μ_5 are synthesized as

$$\begin{aligned}
\mu_4 &= \xi_7 s_4 + \xi_8 |s_4|^{0.5} \operatorname{sgn}(s_4) + \eta_4 \operatorname{sgn}(s_4),\\
\mu_5 &= \xi_9 s_5 + \xi_{10} |s_5|^{0.5} \operatorname{sgn}(s_5) + \eta_5 \operatorname{sgn}(s_5),
\end{aligned} \tag{36}$$

where ξ_7, ξ_8, ξ_9, ξ_{10}, η_4, and η_5 are all positive constants.

If η_5 and η_6 are selected as $\eta_4 > |a_1\widetilde{d}_2|$, $\eta_5 > D_{2d}$ by conducting the same analysis as the foregoing steps, then $\widetilde{\psi}_2$ and $\widetilde{d}_2$ will successively converge to 0 in finite time t_4 beginning at the initial moment $t = 0$; that is, $\widehat{d}_2$ converges to d_2 in the same time t_4.

Finally, $\widehat{d}_1$, $\widehat{d}_{1d}$, and $\widehat{d}_2$ are all estimated after undergoing a finite time t_r, which satisfies $t_r = \max\{t_1 + t_2 + t_3, t_4\}$. The schematic of the DSMO is illustrated in Figure 3. The diagrams of $\widehat{d}_1$ and $\widehat{d}_{1d}$ are only provided for the limitation of space.

Remark 3. The proposed DSMO first observes the observation error of disturbance instead of disturbance itself, unlike the traditional sliding mode observer [37]. The smaller switch gains η_i, $i = 1, 2, 3, 4$, can be permitted because the observation error is typically less than the upper bound of disturbance, which is beneficial for suppression of chattering.

Remark 4. In the proposed DSMO, the estimation process includes two sequential stages. First, disturbance observation errors were obtained. Second, the finite time convergence of $\widetilde{d}_1$, $\widetilde{d}_{1d}$, and $\widetilde{d}_2$ is ensured. The extra-low-pass filter generally used in the traditional sliding mode observer is not required because the dynamic equations of $\widetilde{d}_1$, $\widetilde{d}_{1d}$, and $\widetilde{d}_2$ possess filtering effects, which can be exploited to smooth chattering.

Remark 5. The linear term and terminal attractor of observation error are added and can guarantee a rapid convergence speed during the whole reaching stage. Then, the switch gains η_i, $i = 1, 2, 3, 4$, are only required to be greater than the observation error or the upper bound of disturbance, thereby contributing to chattering restraint to some extent.

Remark 6. The existing nonlinear [38] and extended disturbance observers [39] can achieve the asymptotic convergence of the observation error only if the derivative of disturbance is equal to 0, whereas the bounded estimation result is only obtained when the derivative of disturbance is bounded. By

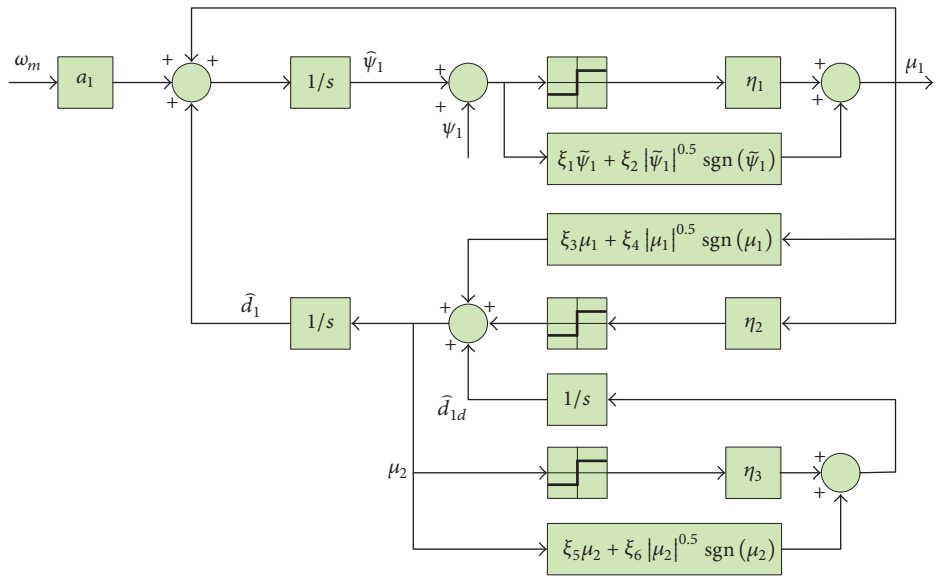

Figure 3: Schematic of the DSMO.

contrast, the presented DSMO can realize the finite time estimation of disturbance and its derivative.

4. Design of a New Sliding Mode Controller (NSMC)

Based on the DSMO proposed in Section 3, a NSMC including a position and a d-axis current controller will be developed in this section.

4.1. Position Sliding Mode Controller. The sliding mode variable σ is reselected as follows:

$$\sigma = e_3 + c_2 e_2 + c_1 e_1 + c_2 \hat{d}_1 + \hat{d}_{1d} + a_1 \hat{d}_2. \tag{37}$$

Control law u_q is designed as

$$u_q = -(a_1 a_2 b_1)^{-1} \left(a_2 a_6 \psi_2 + a_7 \psi_3 - \ddot{x}_d + c_2 e_3 + c_1 e_2 + c_2 \hat{d}_2 + c_1 \hat{d}_1 + c_2 \hat{d}_{1d} + \eta \operatorname{sgn}(\sigma)\right). \tag{38}$$

Here, the following result is obtained.

Theorem 7. *If the sliding mode surface in (37) and control law in (38) are adopted, then sliding mode variable σ can reach the sliding mode surface $\sigma = 0$ in finite time; afterward, position tracking error e_1 will asymptotically converge to 0.*

Proof. First, the reachability of σ will be proven. Taking the derivative of σ along with (20) and substituting (38) into it yield

$$\begin{aligned}
\dot{\sigma} &= \dot{e}_3 + c_2 \dot{e}_2 + c_1 \dot{e}_1 + c_2 \dot{\hat{d}}_1 + \dot{\hat{d}}_{1d} + a_1 \dot{\hat{d}}_2 \\
&= c_2 \tilde{d}_2 + c_1 \tilde{d}_1 + c_2 \hat{d}_{1d} - \eta \operatorname{sgn}(\sigma) + c_2 \left(\mu_2 + \hat{d}_{1d}\right) \\
&\quad + \mu_3 + a_1 \mu_5 \\
&= c_2 \tilde{d}_2 + c_1 \tilde{d}_1 - \eta \operatorname{sgn}(\sigma) + c_2 \mu_2 + \xi_5 \tilde{d}_{1d} \\
&\quad + \xi_6 \left|\tilde{d}_{1d}\right|^{0.5} \operatorname{sgn}\left(\tilde{d}_{1d}\right) + \eta_3 \operatorname{sgn}\left(\tilde{d}_{1d}\right) + a_1 \xi_7 \tilde{d}_2 \\
&\quad + a_1 \xi_8 \left|\tilde{d}_2\right|^{0.5} \operatorname{sgn}\left(\tilde{d}_2\right) + a_1 \eta_5 \operatorname{sgn}\left(\tilde{d}_2\right) \\
&= -\eta \operatorname{sgn}(\sigma) + c_2 \tilde{d}_2 + c_1 \tilde{d}_1 + c_2 \mu_2 + \xi_5 \tilde{d}_{1d} \\
&\quad + \xi_6 \left|\tilde{d}_{1d}\right|^{0.5} \operatorname{sgn}\left(\tilde{d}_{1d}\right) + a_1 \xi_7 \tilde{d}_2 \\
&\quad + a_1 \xi_8 \left|\tilde{d}_2\right|^{0.5} \operatorname{sgn}\left(\tilde{d}_2\right) + \eta_3 \operatorname{sgn}\left(\tilde{d}_{1d}\right) \\
&\quad + a_1 \eta_5 \operatorname{sgn}\left(\tilde{d}_2\right).
\end{aligned} \tag{39}$$

Thus, the Lyapunov function is defined as $V = 0.5\sigma^2$, and then, its derivative is obtained as

$$\begin{aligned}
\dot{V} = \sigma\dot{\sigma} &= -\eta |\sigma| + \sigma \left(c_2 \tilde{d}_2 + c_1 \tilde{d}_1 + c_2 \tilde{d}_{1d} + a_1 \xi_7 \tilde{d}_2 + \xi_5 \tilde{d}_{1d}\right) + \sigma \left(\eta_3 \operatorname{sgn}\left(\tilde{d}_{1d}\right) + a_1 \eta_5 \operatorname{sgn}\left(\tilde{d}_2\right)\right) \\
&\quad + \sigma \left(\xi_6 \left|\tilde{d}_{1d}\right|^{0.5} \operatorname{sgn}\left(\tilde{d}_{1d}\right) + a_1 \xi_8 \left|\tilde{d}_2\right|^{0.5} \operatorname{sgn}\left(\tilde{d}_2\right)\right) \\
&\le -|\sigma| \left(\eta - c_2 \tilde{d}_2 - c_1 \tilde{d}_1 - c_2 \tilde{d}_{1d} - a_1 \xi_7 \tilde{d}_2 - \xi_5 \tilde{d}_{1d} \right. \\
&\quad \left. - \eta_3 - a_1 \eta_5 - \xi_6 \left|\tilde{d}_{1d}\right|^{0.5} - a_1 \xi_8 \left|\tilde{d}_2\right|^{0.5}\right).
\end{aligned} \tag{40}$$

Note that $\tilde{d}_1, \tilde{d}_2$, and $\tilde{d}_{1d}$ will successively converge to zero in finite time t_r, which satisfies $t_r = \max\{t_1 + t_2 + t_3, t_4\}$, then

$$\begin{aligned}
\dot{V} &\le -\eta |\sigma| + |\sigma| (\eta_3 + a_1 \eta_5) = -|\sigma| [\eta - (\eta_3 + a_1 \eta_5)] \\
&= -[\eta - (\eta_3 + a_1 \eta_5)] V^{0.5}.
\end{aligned} \tag{41}$$

Evidently, σ will converge to 0 in finite time if η is selected such that $\eta > \eta_3 + a_1\eta_5$.

Next, it is proved that e_1 will asymptotically converge to 0, and the dynamic performance of e_1 depends on $\sigma = 0$ after σ reached the sliding mode surface $\sigma = 0$; that is,

$$\begin{aligned} &e_3 + c_2e_2 + c_1e_1 + c_2\widehat{d}_1 + \widehat{d}_{1d} + a_1\widehat{d}_2 \\ &\quad = \ddot{e}_1 + c_2\dot{e}_1 + c_1e - c_2d_1 - \dot{d}_1 - a_1d_2 + c_2\widehat{d}_1 + \widehat{d}_{1d} \\ &\qquad + a_1\widehat{d}_2 = 0. \end{aligned} \tag{42}$$

The simplification of (42) can be expressed as

$$\ddot{e}_1 + c_2\dot{e}_1 + c_1e = c_2\widetilde{d}_1 + \widetilde{d}_{1d} + a_1\widetilde{d}_2. \tag{43}$$

According to the results presented in Section 3, $\widetilde{d}_1, \widetilde{d}_2$, and $\widetilde{d}_{1d}$ will all converge to 0 in finite time and consider that c_1, c_2 are Hurwitz; obviously, the position tracking error e_1 is asymptotic stability. □

Remark 8. The mismatched disturbances that are transformed into matched ones are not adopted in this work to handle mismatched disturbances d_1 and d_2, because doing that will result in undesired consequences, where the velocity $\dot{x}$ and the acceleration $\ddot{x}$ will be required when constructing sliding mode surface. Thus, the extra state observer must be designed, whereas to the proposed NSMC that is expressed in (18), (20), and (37), all state variables (i.e., x, ω_m, i_q) are measurable. Therefore, the state observer will be avoided to use.

Remark 9. In the proposed NSMC, mechanical, hydraulic subsystems and IEHP are considered a synthesis in which control law u_q can be directly acquired, which is highly distinct from the existing SMC design methods of the EHSAS. In addition, the estimated disturbances are also added to u_q to alleviate chattering in a feed forward way in addition to compensating the mismatched disturbances.

Remark 10. Although e_1 displays asymptotic convergence, e_2 and e_3 cannot converge to 0, thereby satisfying the following relationships:

$$\begin{aligned} \lim_{t\to\infty} e_2 &= -d_1 \\ \lim_{t\to\infty} e_3 &= a_1d_2 + \dot{d}_1. \end{aligned} \tag{44}$$

4.2. d-Axis Current Sliding Mode Controller. The d-axis current of the IEHP is assumed to adopt $i_d^* = 0$ form of vector control. Thus, the sliding variable is defined as

$$s_d = e_d = i_d - i_d^*. \tag{45}$$

Taking the derivative of s_d and substituting (1) into it yield

$$\dot{s}_d = \frac{pL_q}{L_d}x_4x_5 - \frac{R}{L_d}x_6 + \frac{u_d}{L_d}. \tag{46}$$

The CRRL is selected; that is, $\dot{s}_d = -\eta_d \operatorname{sgn}(s_d)$. Thus, the following equation is easily obtained:

$$u_d = -L_d\left(\frac{pL_q}{L_d}x_4x_5 - \frac{R}{L_d}x_6 + \eta_d \operatorname{sgn}(s_d)\right), \tag{47}$$

where $\eta_d > 0$ is switch gain.

5. NARL

The SMC includes the sliding motion and reaching stage two parts and the reaching law method is prevailing to ensure the reachability of the sliding mode variable. In general, the reaching stage not only requires faster reaching rate but also maintains smaller chattering magnitude.The CRRL used in the previous section is commonly employed, nevertheless, which is difficult to reconcile the contradiction between reaching speed and chattering. In this section, a NARL will be introduced to handle this conflict and compared with several commonly used reaching laws for exhibiting its advantages. For ease of analysis, a double integrator system is selected as the study object; that is, $\dot{x}_1 = x_2$, $\dot{x}_2 = u$, where u is the control input, and the sliding mode variable is designed as $\sigma = x_2 + cx_1$. The following reaching laws are adopted.

5.1. CRRL. The CRRL can be denoted as follows:

$$\dot{\sigma} = -\eta \operatorname{sgn}(\sigma). \tag{48}$$

Integrating (48) with respect to time, then the time t_{a1} of σ reaching the sliding mode surface can be obtained by

$$t_{a1} = \frac{|\sigma(0)|}{\eta}, \tag{49}$$

where $\sigma(0)$ is the initial value of σ at $t = 0$.

From the view of discrete system, the amplitude width of the chattering near the sliding surface can be acquired approximately. The sample period is assumed as T_s. Then, (48) can discretize the following form through Euler method:

$$\sigma(k+1) = \sigma(k) - T_s\eta \operatorname{sgn}\sigma(k), \tag{50}$$

where $\sigma(k) = 0^+$ denotes the limiting value of $\sigma(k)$ approaching zeros from the $\sigma > 0$ region and $\sigma(k) = 0^-$ represents the limiting value of $\sigma(k)$ approaching zeros from the $\sigma < 0$ region. Thus, the resulting values of σ in the next sample period are $T_s\eta$ and $-T_s\eta$, respectively, thereby implying that σ will eventually chatter in a range from $-T_s\eta$ to $T_s\eta$, and this chattering bandwidth Δ_1 can be calculated as

$$\Delta_1 = 2T_s\eta. \tag{51}$$

In Figure 4(a), the shape of the chattering region of the CRRL is a rectangle, which means that the state x_1 cannot converge to 0. In addition, (49) indicates that the larger switch gain η must be chosen if the smaller t_{a1} wants to be achieved, and then the chattering bandwidth will be further enlarged. Therefore, the CRRL cannot solve the contradiction between reaching speed and chattering.

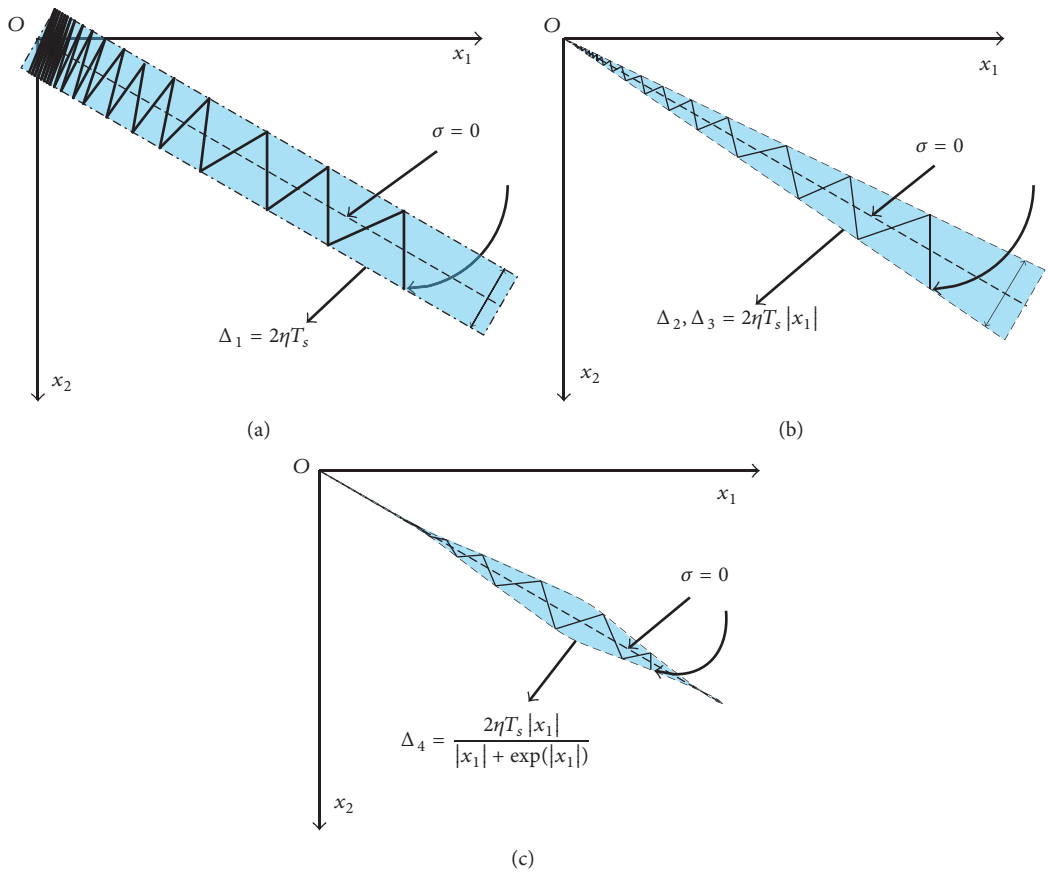

FIGURE 4: Phase trajectories. (a) CRRL. (b) TVRRL and IVRRL. (c) Proposed adaptive reaching law.

5.2. Traditional Variable Rate Reaching Law (TVRRL). Another reaching law that is used frequently is TVRRL, which can be expressed as

$$\dot{\sigma} = -\eta |x_1| \operatorname{sgn}(\sigma). \tag{52}$$

Similarly, the reaching time t_{a2} and the chattering bandwidth Δ_2 of the TVRRL can be expressed as

$$t_{a2} = \frac{|\sigma(0)|}{\eta |x_1|}, \tag{53}$$

$$\Delta_2 = 2T_s \eta |x_1|. \tag{54}$$

In (53) and (54), t_{a2} and Δ_2 are related to state x_1 compared with the CRRL. The advantages of the TVRRL lie in the following: the reaching rate will increase if $|x_1|$ is larger; moreover, $|x_1|$ and Δ_2 will all gradually approach 0 with the sliding mode motion proceeding after σ reached the sliding surface. However, the reaching rate will also be slowed with the decrease of $|x_1|$, and the severe chattering may occur if $|x_1|$ maintains a larger value during the initial stage of the sliding motion. Note that from Figure 4(b) the shape of the TVRRL chattering domain appears to be triangular.

5.3. Improved Variable Rate Reaching Law (IVRRL). Recently, the IVRRL is developed in [40], which can be expressed as

$$\dot{\sigma} = \frac{-\eta |x_1|}{\beta + (1-\beta)\exp(-\alpha |\sigma|)} \operatorname{sgn}(\sigma), \tag{55}$$

where $\alpha \geq 1$, $0 < \beta \leq 1$.

Similarly, the corresponding reaching time t_{a3} and chattering bandwidth Δ_3 will be obtained as

$$t_{a3} = \frac{1}{\eta |x_1|}\left[\beta |\sigma(0)| + \frac{1-\beta}{\alpha}\left(1 - \exp(-\alpha |\sigma(0)|)\right)\right], \tag{56}$$

$$\Delta_3 = 2T_s \eta |x_1|. \tag{57}$$

The IVRRL can dynamically adjust the switch gain η between $\eta|x_1|$ and $\eta|x_1|/\beta$ compared with the TVRRL. The smaller η can be selected under the same reaching speed, and then the chattering is suppressed to some extent. However, the deficiencies in the TVRRL remain; thus, the reaching speed is affected by state x_1 and the dramatic chattering in the incipient phase of the sliding mode. In Figure 4(c), the shape of the IVRRL chattering band is the same as that of the TVRRL.

5.4. NARL. NARL is proposed to solve the problems in the aforementioned reaching laws and can be designed by

$$\begin{aligned}\dot{\sigma} &= \frac{-\eta}{\beta + (1-\beta+\exp(|x_1|)/|x_1|)\exp(-\alpha|\sigma|)}\operatorname{sgn}(\sigma) \\ &= -f(\sigma, x_1)\operatorname{sgn}(\sigma),\end{aligned} \tag{58}$$

where $\alpha \geq 1$, $0 < \beta \leq 1$.

The reaching time t_{a4} and the chattering bandwidth Δ_4 can be formulated by

$$\begin{aligned}t_{a4} = \frac{1}{\eta}\Bigg[\beta|\sigma(0)| + \left(\frac{1-\beta}{\alpha} + \frac{\exp(|x_1|)/|x_1|}{\alpha}\right) \\ \cdot (1 - \exp(-\alpha|\sigma(0)|))\Bigg],\end{aligned} \tag{59}$$

$$\Delta_4 = \frac{2\eta T_s |x_1|}{|x_1| + \exp(|x_1|)}. \tag{60}$$

In (58), the switch gain $f(\sigma, x_1)$ will tend to η/β when σ is far from the sliding surface, and $f(\sigma, x_1)$ approaches $\eta|x_1|/(|x_1| + \exp(|x_1|))$ when σ is near the sliding surface $\sigma = 0$. Thus, the NARL can also realize an adaptive regulation in response to the distance from the sliding surface. In (59), because $1 - \exp(-\alpha|\sigma(0)|) \leq 1$ and $(1-\beta)/\alpha + (\exp(|x_1|)/|x_1|)/\alpha \geq 0$; thus, if α is selected as $\alpha \gg 1 - \beta + \exp(|x_1|)/|x_1|$, then the following relationship can be deduced by

$$t_{a4} < \frac{\beta|\sigma(0)|}{\eta} < t_{a1}. \tag{61}$$

Compared with the CRRL, η/β is much greater than η, thereby indicating that the faster reaching speed will be available even when using the same η. The smaller η will be permitted from another perspective, with the same reaching rate, and thus the chattering will be more effectively attenuated. Compared with TVRRL and IVRRL, the reaching speed of the NARL is unaffected by state x_1. Moreover, since $0 \leq |x_1|/(|x_1| + \exp(|x_1|)) \leq 1$, the severe chattering problem during the initial sliding motion is avoided. In addition, the bandwidth of the NARL is also less than that of the CRRL, TVRRL, and IVRRL by observing (51), (54), (57), and (60). In Figure 4(d), the shape of the NARL chattering band is fusiform. In addition, since $f(\sigma, x_1) > 0$ in (58), the reachability condition is automatically satisfied.

Thus, the CRRL in (38) and (47) is replaced by the NARL, and the new control laws can be formulated as

$$\begin{aligned}u_q = &-(a_1a_2b_1)^{-1}\Big(a_2a_6\psi_2 + a_7\psi_3 - \dddot{x}_d + c_2e_3 + c_1e_2 \\ &+ c_2\hat{d}_2 + c_1\hat{d}_1 + c_2\hat{d}_{1d} + f(\sigma, e_1)\operatorname{sgn}(\sigma)\Big), \\ u_d = &-L_d\left(\frac{pL_q}{L_d}x_4x_5 - \frac{R}{L_d}x_6 + f(s_d)\operatorname{sgn}(s_d)\right),\end{aligned} \tag{62}$$

Table 1: Simulation parameters.

Parameter	Value
ψ_f	0.12 Wb
J	$5e-4$ kg·m^2
D	$3.97e-7$ m^3/rad
B_m	$6e-4$ Nm/rad/s
A	$1.13e-3$ m^2
V_t	$4.0e-4$ m^3
m_c	2.9 kg
m_L	5.0 kg
C_t	$2.50e-11$ m^3/s/pa
β_e	$6.86e+8$ N/m^2
B_c	1000 N/m/s
Maximum stroke	0.1 m
Maximum output force	20 kN
Maximum speed of the IEHP	1000 rad/s

where

$$\begin{aligned}f(\sigma, e_1) &= \frac{-\eta}{\beta + (1-\beta+\exp(|e_1|)/|e_1|)\exp(-\alpha|\sigma|)}, \\ f(s_d) &= \frac{-\eta_d}{\beta + (1-\beta+\exp(|s_d|)/|s_d|)\exp(-\alpha|s_d|)}.\end{aligned} \tag{63}$$

The whole position control block diagram of the EHSAS is illustrated in Figure 5.

6. Simulations and Analysis

The cosimulation platform of the EHSAS is constructed by utilizing AMESim and MATLAB/Simulink to verify the feasibility and effectiveness of the proposed NSMC method. Hydraulic, mechanical subsystems and IEHP are set up with AMESim, and the DSMO, NARL, and NSMC are implemented with MATLAB/Simulink. The cosimulation model is depicted in Figure 10. The proposed NSMC is compared with three-loop PID method, which is widely adopted in the control of the EHSAS. The related system parameters are listed in Table 1. In the simulation, using symbol SMC represents the method mentioned in Section 3, where the mismatched disturbances are uncompensated.

Each control loop of the three-loop PID all uses PI controller, in which the proportional and integral gains of position loop are $K_{xp} = 10000$, $K_{xi} = 20000$; the speed parameters of the IEHP are set as $K_{vp} = 1.5$, $K_{vi} = 2$, $K_{qp} = 10$, $K_{qi} = 200$, and the parameters of the d-axis current loop are $K_{dp} = 25$, $K_{di} = 900$. The related parameters of the NSMC are selected as $c_1 = 3600$, $c_2 = 400$, $\eta = 600$, $\beta = 0.05$, $\alpha = 10$. The parameters of the DSMO are $\eta_1 = 0.01$, $\xi_2 = 10$, $\eta_2 = 0.05$, $\xi_3 = 50$, $\xi_1 = 7$, $\xi_4 = 60$, $\eta_3 = 0.5$, $\xi_5 = 30$, $\xi_6 = 20$, $\eta_4 = 1$, $\xi_7 = 50$, $\xi_8 = 30$, $\eta_5 = 100$, $\xi_9 = 90000$, $\xi_{10} = 80000$. For convenience, the three-loop PID method is denoted by PID in the sequel. Simulations are performed in the following cases.

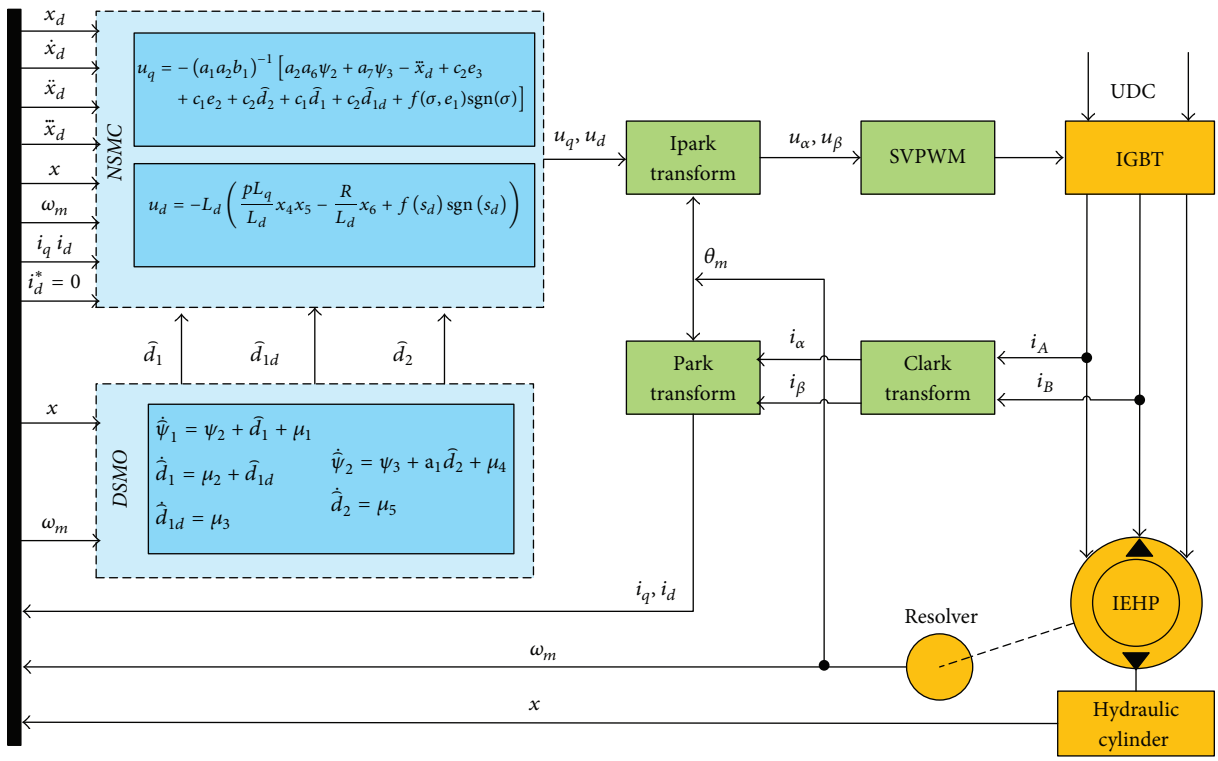

FIGURE 5: Complete control block diagram of the EHSAS.

Case 1 (verify the effectiveness of the NARL). First, the validity of the NARL is demonstrated by comparative simulations with reaching laws mentioned in Section 5. For simplicity, a double integrator system is still selected as the analysis object, that is, $\dot{x}_1 = x_2$, $\dot{x}_2 = u$, and state initial values are assumed as $x_1(0) = 10$ and $x_2(0) = 10$. Similarly, the sliding variable $\sigma = x_2 + cx_1$ is selected, and the reaching laws introduced in Section 5 are used. Then, the resulting control law u can be obtained by CRRL:

$$u = -cx_2 - \eta\,\mathrm{sgn}(\sigma); \tag{64}$$

TVRRL:

$$u = -cx_2 - \eta|x_1|\,\mathrm{sgn}(\sigma); \tag{65}$$

IVRRL:

$$u = -cx_2 - \frac{-\eta|x_1|}{\beta + (1-\beta)\exp(-\alpha|\sigma|)}\,\mathrm{sgn}(\sigma); \tag{66}$$

NARL:

$$u = -cx_2 - \frac{-\eta}{\beta + (1-\beta+\exp(|x_1|)/|x_1|)\exp(-\alpha|\sigma|)} \cdot \mathrm{sgn}(s). \tag{67}$$

The simulation results are presented in Figures 6–9, in which (a) is the system state response curve, (b) displays the sliding variable σ convergence curves, (c) depicts the control output u, and (d) illustrates the phase trajectories. For the CRRL, the related parameters are set as $\eta = 50, c = 1$. In Figures 6(a) and 6(b), x_1, x_2, and σ are unable to approach 0, although they are convergent. Moreover, the severe chattering phenomenon occurred in σ and u, as demonstrated in Figures 6(b) and 6(c); particularly, the chattering amplitude of u has reached ±50. In Figure 6(d), the shape of the CRRL chattering band is rectangular. In terms of the TVRRL, the same parameters are selected as $\eta = 50$, $c = 1$. σ and u exhibit drastic chattering during the initial stage of the sliding mode, although the reaching speed is increased because of adding $|x_1|$, and x_1, x_2, and σ can also be guaranteed to converge to 0, as depicted in Figures 7(b) and 7(c). The maximum amplitude chattering of u has increased to ±500, which is far greater than that of the CRRL. In Figure 7(d), the chattering band appears triangular.

A smaller η in the IVRRL than in the TVRRL can be selected with the same reaching speed given the dynamic adjustment of switch gain. Thus, η is set as $\eta = 5$, and other parameters are set as $\beta = 0.5$, $\alpha = 10$. In Figures 8(b) and 8(c), the maximum amplitude chattering of u still reaches up to ±200 in the sliding mode initial stage, although chattering is suppressed given the decrease of η. Similarly, the shape of the IVRRL chattering band depicted in Figure 8(d) is an approximate triangle. The parameters of the NARL maintain the same values; that is, $\eta = 5$, $\beta = 0.5$, $\alpha = 10$. In Figures 9(b) and 9(c), the NARL achieves not only the same reaching speed by using the smaller η than the CRRL but also chattering problem in the TVRRL

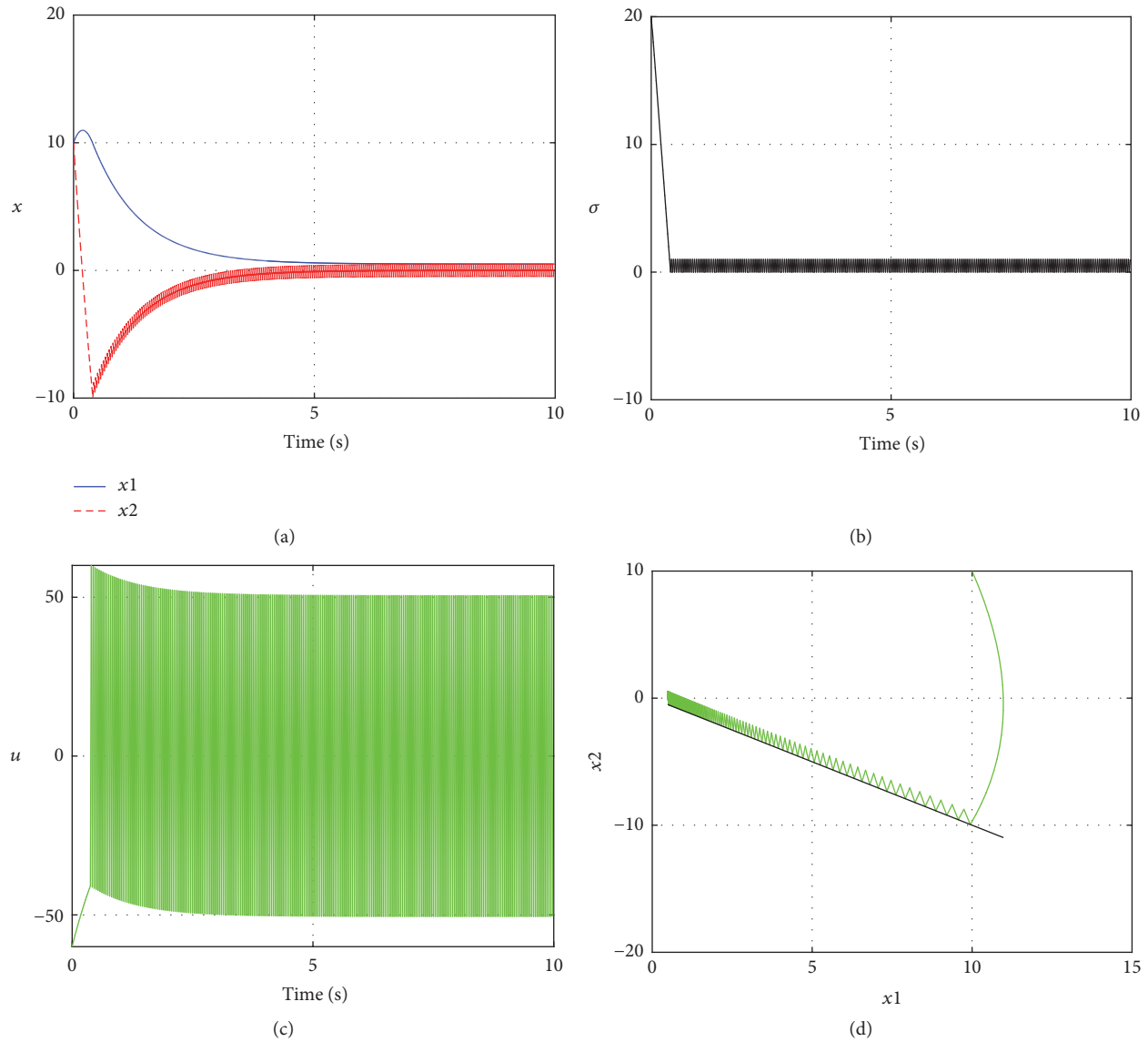

FIGURE 6: Performance of the CRRL. (a) State response. (b) Sliding mode surface convergence process. (c) Control output. (d) Phase trajectory.

and IVRRL during the sliding mode initial phase is avoided. Control signal u and sliding variable σ are quite smooth throughout the sliding phase, and the chattering bandwidth of the NARL is significantly less than the CRRL, TVRRL, and IVRRL. Moreover, Figure 9(c) illustrates that the shape of the chattering band is fusiform, which is consistent with the analysis presented in Section 5.

Case 2 (step signal tracking performance). The desired position step signal is presented as $x_d = 0.02$ m at $t = 0$ s; then, x_d is changed to $x_d = 0.08$ m at $t = 4$ s, and no external load is applied on the EHSAS. The position step response curves of the PID and NSMC are depicted in Figure 11(a). In this figure, regardless of whether small or large step reference signal, the PID generates approximately 15% overshoot, whereas the NSMC can achieve nonovershoot performance, and the settling time is obviously smaller than that of the PID.

The position step reference is set to $x_d = 0.08$ m at $t = 0$ to further verify the disturbance rejection capability of the NSMC, and the step-type external load force $F_L = 1 \times 10^3$ N is suddenly exerted at $t = 4$ s. In Figure 11(b), although PID can eventually compensate this step disturbance, the compensation speed is quite dilatory in which the maximum position difference between the desired and the actual values has reached 0.04 m, which accounts for approximately 50% of the desired value. By contrast, the maximum position difference is only 0.004 m, and disturbance is swiftly compensated when using the NSMC. Actually, PID compensates disturbance through integral action; hence, the lagged effect of compensation is inevitable. This effect may result in the larger overshoot in the case of no disturbance, although this effect can be ameliorated by increasing the value of position loop integral gain K_{xi}. The disturbance rejection of the NSMC is achieved by utilizing switch gain η and DSMO,

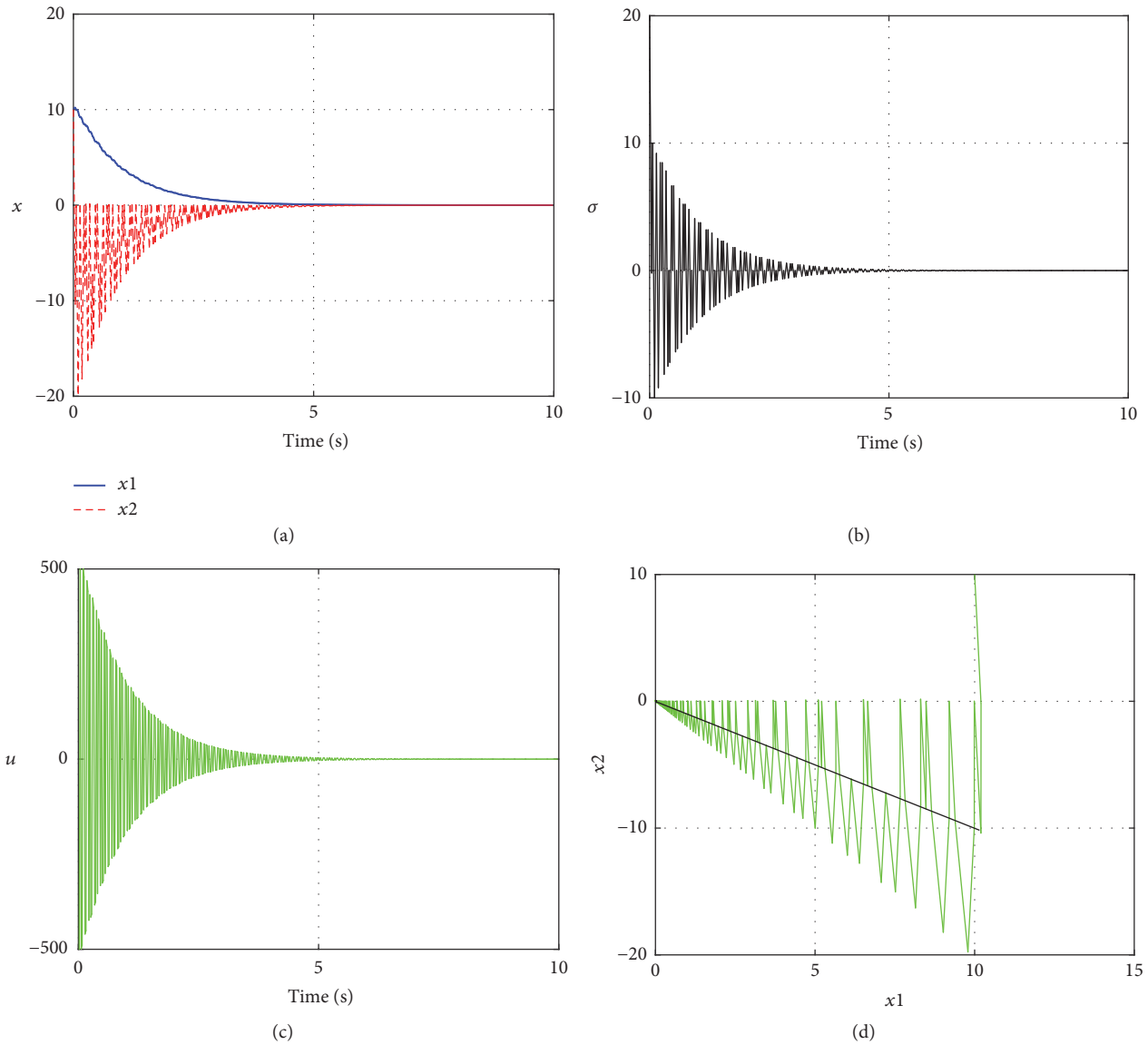

FIGURE 7: Performance of the TVRRL. (a) State response. (b) Sliding mode surface convergence process. (c) Control output. (d) Phase trajectory.

which is similar to a feedforward compensation method; thus, the antidisturbance effect is necessarily superior to PID. In addition, Figure 11(b) indicates that the SMC has no compensation capability to mismatch disturbance. Moreover, the DSMO is similar to a patch such that the disturbance can be effectively compensated in the presence of disturbance but has no adverse effect on the performance in absence of disturbance. In Figures 11(c)-11(d), disturbances d_1 and d_2 and the derivative of d_1 can be estimated exactly, and undesired chattering does not appear. The switch gain η of the CRRL under the condition of the same reaching speed is $\eta = 60000$ and that of NARL is 600, it can be illustrated in Figure 11(f) that the control signal u_q of NARL is very smooth, whereas that of the CRRL has large chattering.

The step-type disturbance is replaced by a sinusoidal-type external load force, namely, $F_L = 1 \times 10^3 \sin(4\pi t)$ N, to be closer to the actual situation. The corresponding results are illustrated in Figure 12; we can find that the NSMC still achieves a satisfying result in terms of disturbance compensation capability, estimation accuracy of disturbance, and suppression chattering. It is should be noted that the PID cannot compensate this sinusoidal disturbance; in fact, the integral action of PID can only handle slow- varying disturbance and can be useless to fast time- varying period disturbance. In addition, Figure 12(e) depicts the response result of the d-axis current, where the curve of the NSMC is stable throughout the response process, whereas PID displays several fluctuations.

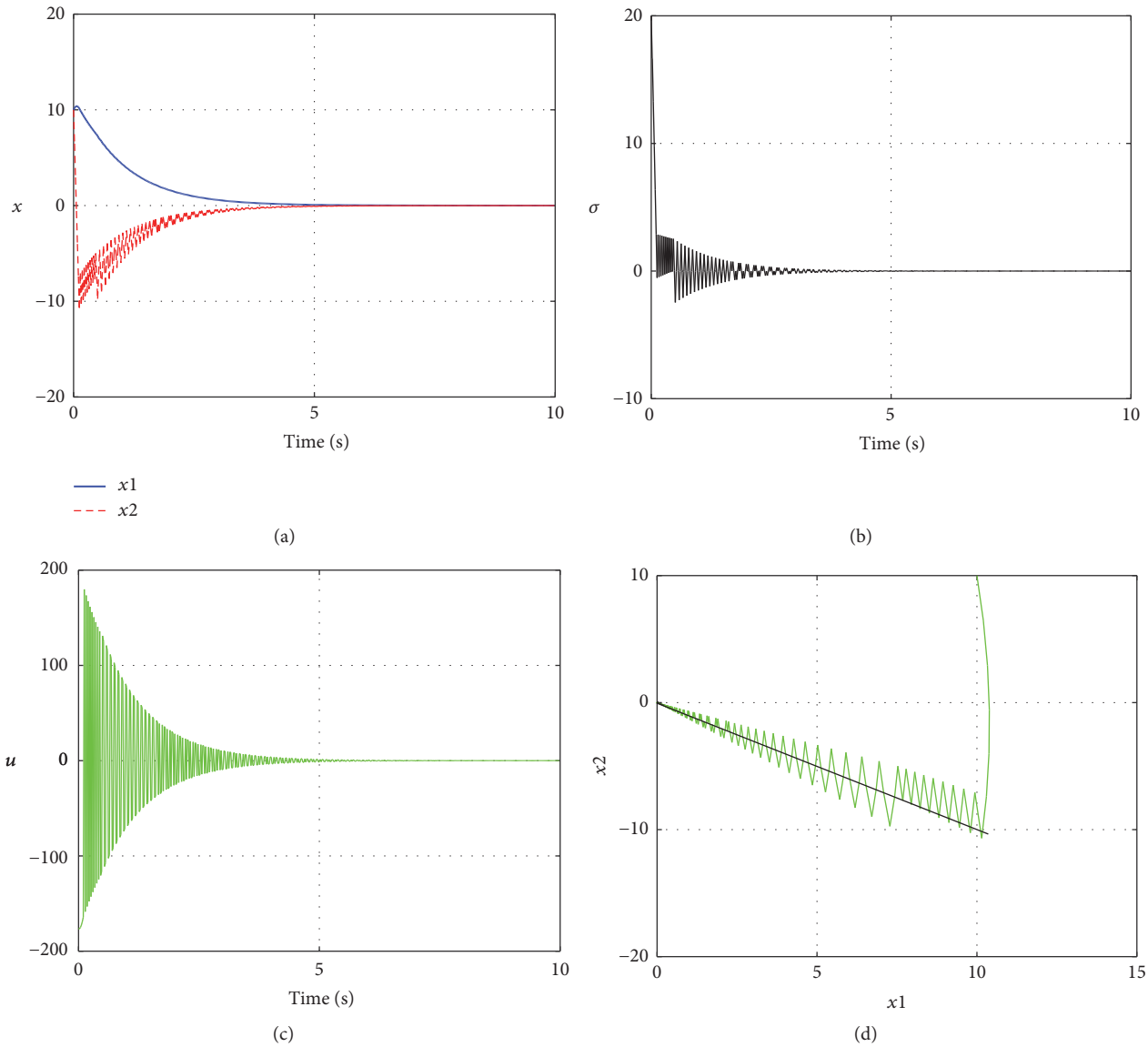

FIGURE 8: Performance of the IVRRL. (a) State response. (b) Sliding mode surface convergence process. (c) Control output. (d) Phase trajectory.

Therefore, the disturbance rejection capability of the NSMC significantly outperforms PID and SMC; the proposed sliding mode design architecture is feasible and effective.

Case 3 (sinusoidal signal tracking performance). Frequency bandwidth is an important performance index that is used to evaluate the rapidness and accuracy of the control system, that is, the tracking performance of sinusoidal signal with different frequency. To this end, the position reference signal is arranged as $x_d = 5 \times 10^{-3} \sin(2\pi t)$ m at $t = 0$ s and then changed to $x_d = 5 \times 10^{-3} \sin(6\pi t)$ m at $t = 3$ s; then, this signal is set to $x_d = 5 \times 10^{-3} \sin(12\pi t)$ m at $t = 6$ s, which is used to simulate low, intermediate, and high-frequency desired position signal, respectively. Moreover, no external load is exerted on the EHSAS. Figure 13 reveals that PID and NSMC achieve a satisfying tracking performance, and the tracking error remains smaller in the NMSC than in the PID. Furthermore, the position tracking curve of the PID appears as a flat-top phenomenon at the place of maximal position, which is caused by nonlinear friction. By contrast, the same problem is overcome in the NSMC to some extent, which is contributed to the estimation and compensation of the DSMO to disturbance d_1. Next, more complicated situations are considered to further test the antidisturbance capability. A flexible load with stiffness coefficient $K_s = 6 \times 10^5$ N/m is added to simulate the internal perturbation; moreover, sinusoidal load force is exerted with an amplitude of 1000 N and frequency of 2 Hz to simulate external disturbance. In

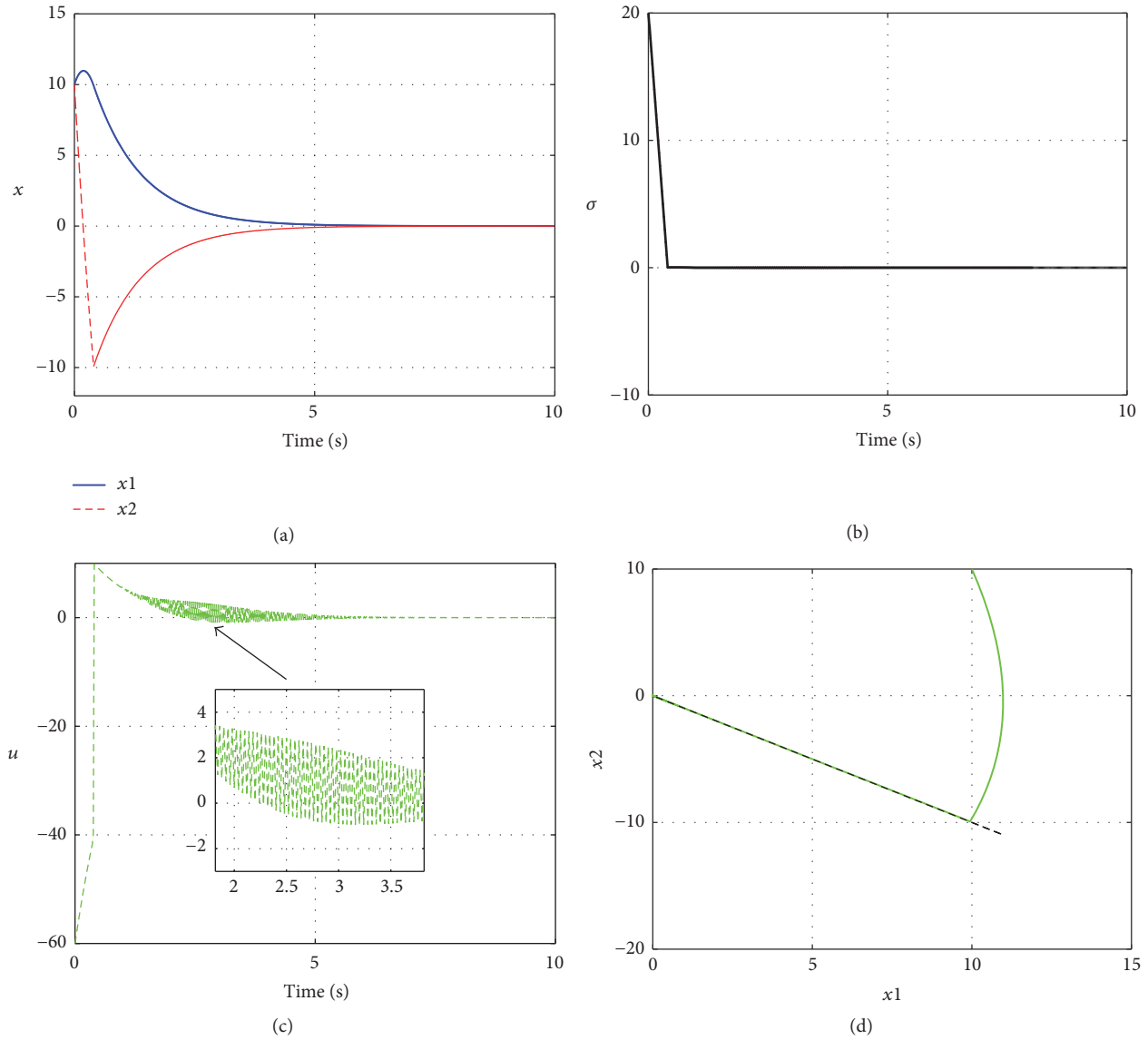

FIGURE 9: Performance of the NARL. (a) State response. (b) Sliding mode surface convergence process. (c) Control output. (d) Phase trajectory.

this case, Figure 14 demonstrates that the PID tracking performance is obviously deteriorated, but the NSMC still manifests a favorable control performance.

Case 4 (robustness to parameter variation). In practice, the load mass m_L and the leakage coefficient C_t will vary with the change of load and working conditions, such as oil temperature, wear, and seal. Thus, m_L and C_t are changed as $m_L = 100\,\text{kg}$ and $C_t = 2.5 \times 10^{-12}\,\text{m}^3/\text{s/pa}$, respectively, to validate the robustness of the NSMC to parametric variation. The parameter η is increased as $\eta = 2000$ to enhance the robustness of the NSMC, to be fair, the position loop proportional gain K_{xp} of PID is also increased to 30000, and the rest of the parameters remain unchanged. Figure 15 indicates that the PID nearly cannot track the given position signal and accompanies severe resonance oscillation phenomenon, with respect to the NSMC, the result remains acceptable despite the slight degradation of tracking accuracy. Therefore, the robustness of the NSMC to parametric variation is much better than PID. The reason for this phenomenon will be analyzed as follows.

In (13), the transfer function between ω_m and x can be deduced as

$$\frac{X(s)}{\omega_m(s)} = \frac{(D/A) \bullet \left(4\beta_e A^2/MV_t\right)}{s\left(s^2 + \left(2\beta_e C_t/V_t\right)s + 2\beta_e A^2/MV_t\right)}, \tag{68}$$

where $\omega_n = \sqrt{4\beta_e A^2/MV_t}$, $\zeta = (\beta_e C_t/V_t) \bullet (1/\omega_n) = (\beta_e C_t/V_t)\sqrt{MV_t/2\beta_e A^2}$, ω_n denotes the hydraulic natural frequency, and ζ represents the hydraulic damping ratio.

The damping ratio ζ equals 0.04 when m_L and C_t are $m_L = 100\,\text{kg}$, $C_t = 2.5 \times 10^{-12}\,\text{m}^3/\text{s/pa}$. It is well known

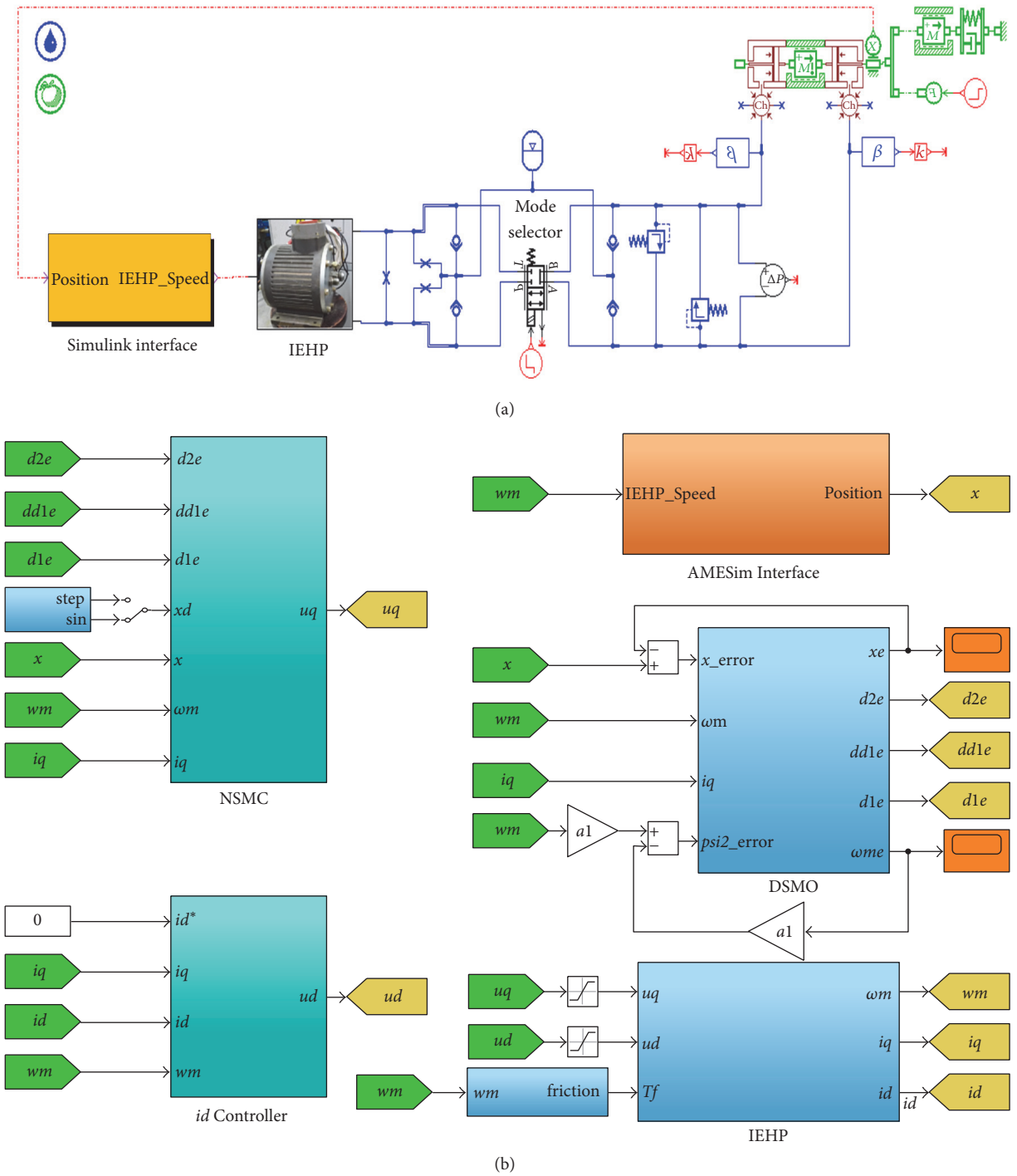

FIGURE 10: Cosimulation model of the EHSAS. (a) Hydraulic and mechanical submodel in AMESim. (b) NSMC and SMO in MATLAB/Simulink.

that the resonance peak will be generated when the damping ratio ζ is less than 0.707; thus, the large resonance peak will certainly occur. In the formulas of ω_n and ζ, ω_n and ζ will be decreased with the increase of m_L and decrease of C_t, which eventually lead to the significant reduction of magnitude margin (GM). For the PID, the GM will be further decreased with the increase of K_{xp}, which inevitably results in system oscillation and even instability. For the NSMC, because d_1 includes the information of acceleration $\ddot{x}$, which is able to increase the hydraulic damping ratio, oscillation is restrained to some extent when d_1 is added to the control law by estimating DSMO.

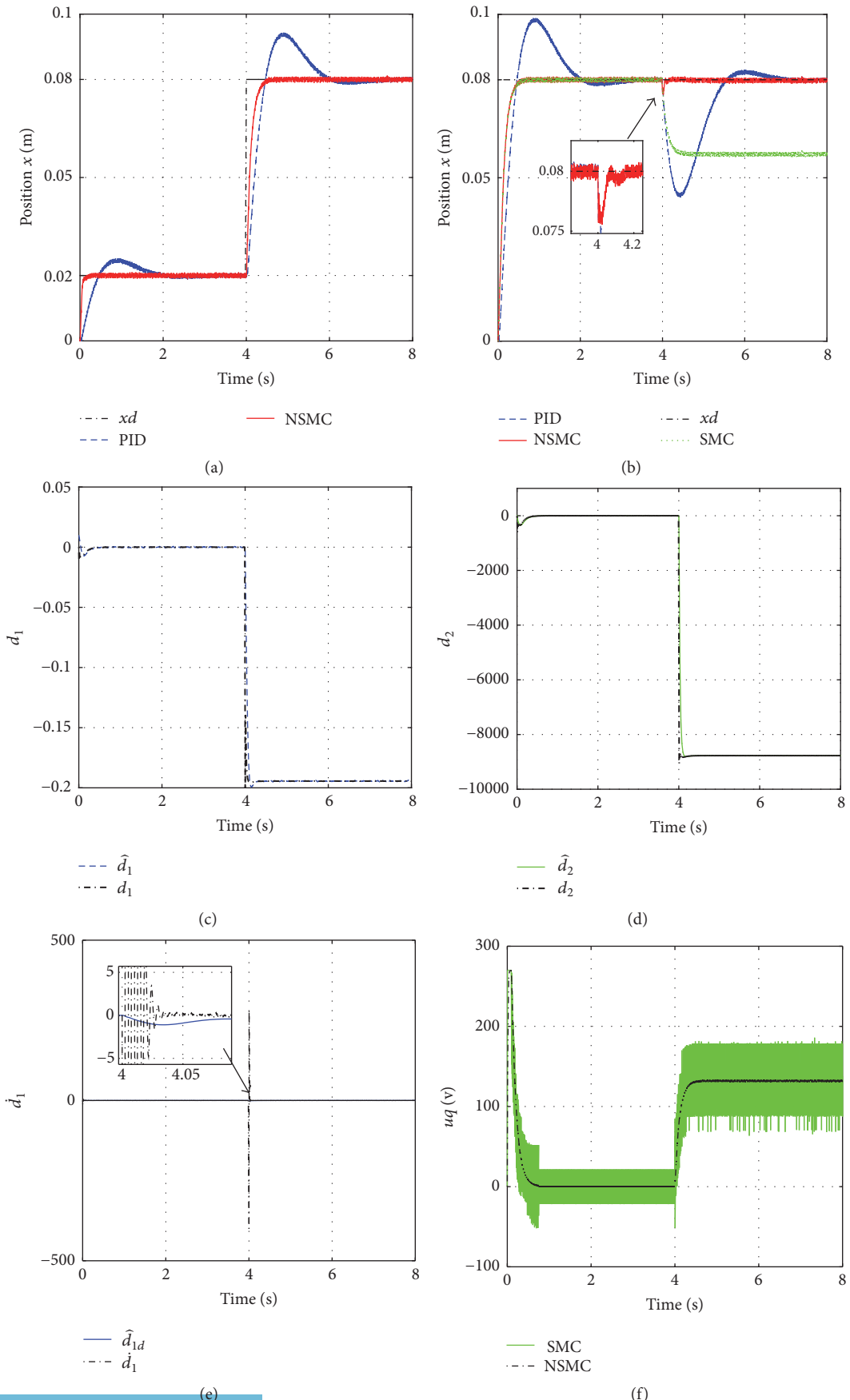

FIGURE 11: Position step response under no load and step disturbance. (a) Step response in the case of no load. (b) Step response in the case of step disturbance. (c) Estimation of d_1. (d) Estimation of d_2. (e) Estimation of $\dot{d}_1$. (f) Control output.

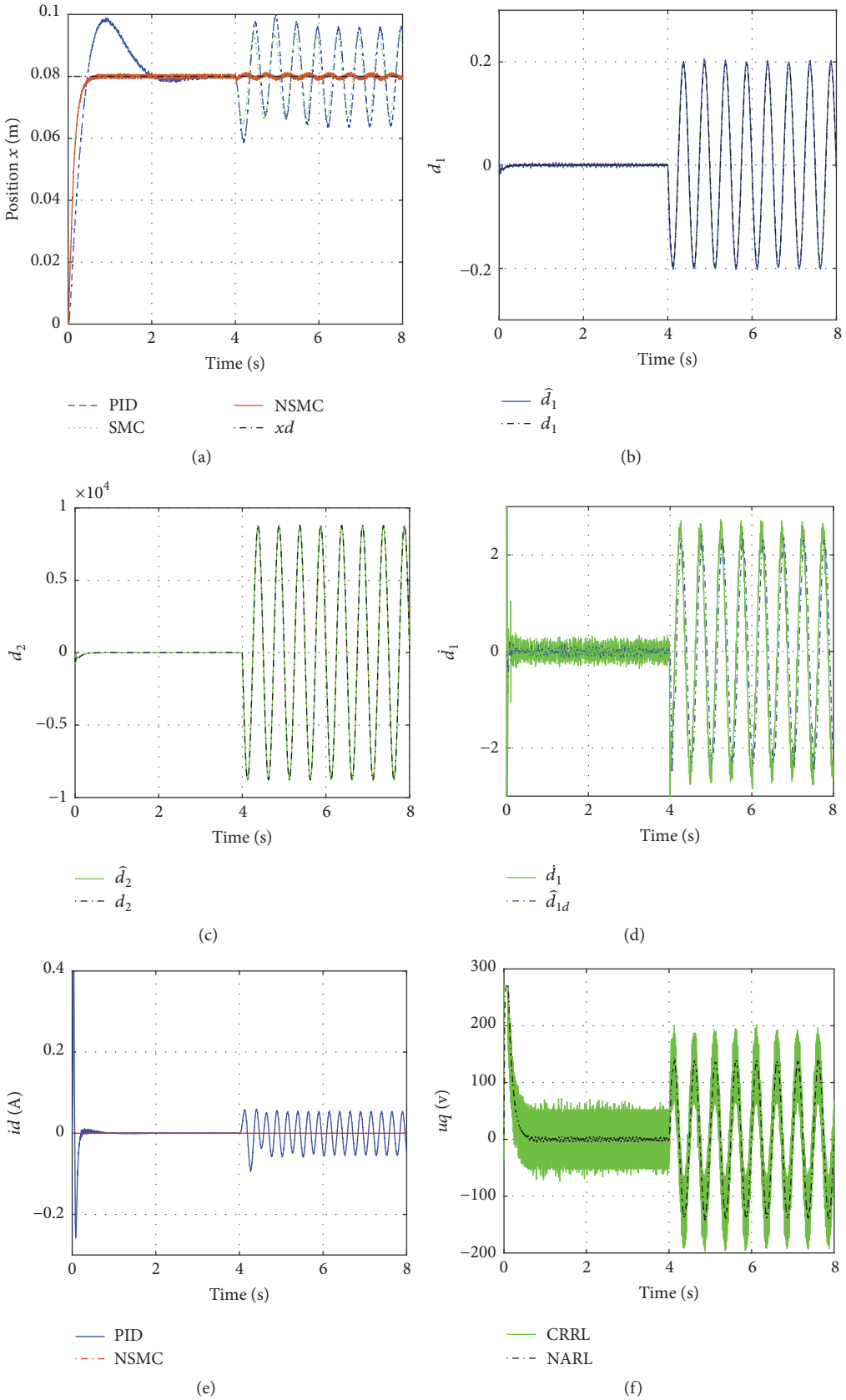

FIGURE 12: Position step response under sinusoidal disturbance. (a) Step response in the case of a sinusoidal disturbance. (b) Estimation of d_1. (c) Estimation of d_2. (d) Estimation of $\dot{d}_1$. (e) i_d response curve. (f) Control output.

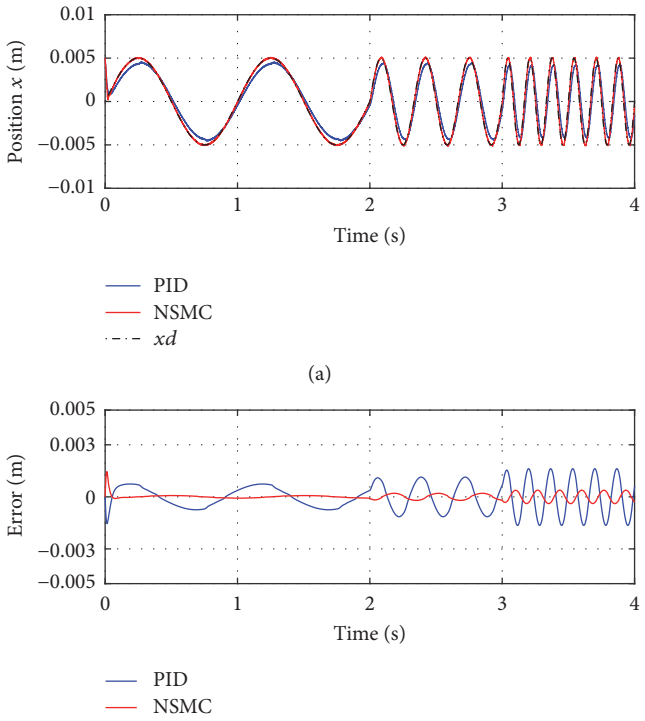

Figure 13: Position tracking performance to a sinusoidal signal in the case of no load. (a) Position tracking performance. (b) Tracking error.

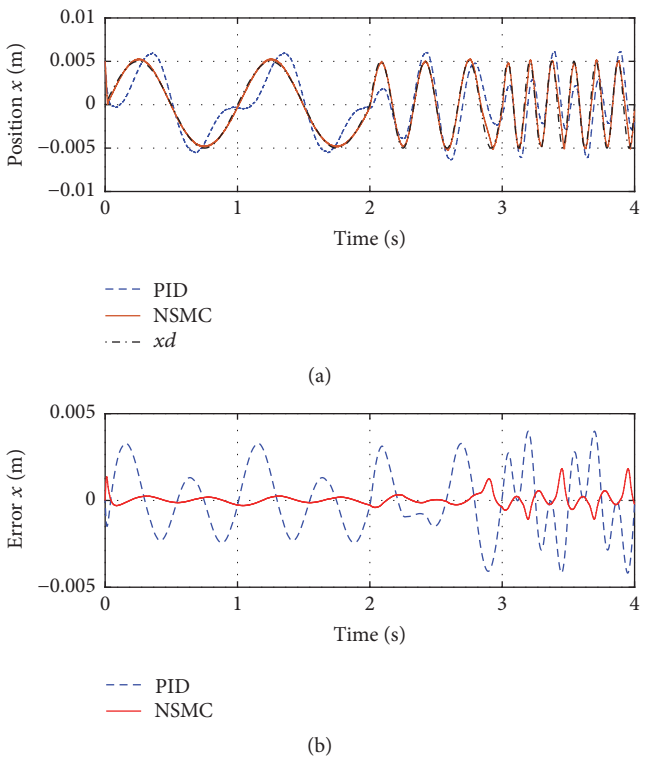

Figure 14: Position tracking performance to a sinusoidal signal in the case of a complicated disturbance. (a) Position tracking performance. (b) Tracking error.

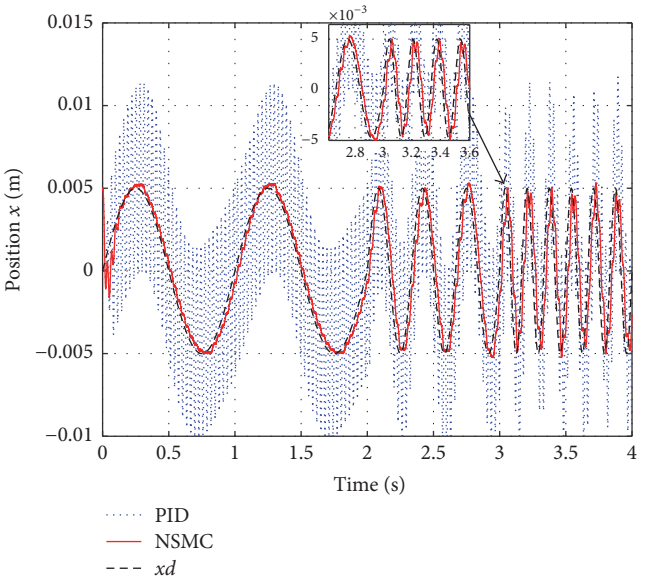

Figure 15: Position tracking performance to sinusoidal signal in the case of parameter variation.

7. Conclusions

In this work, a unique SMC architecture is proposed for electrohydrostatic position actuation system, which possesses many prominent superiorities, such as excellent simplification of the design process, avoidance of state observer, effective compensation of mismatched disturbance, and remarkable effect of chattering suppression compared with the traditional SMC. The validity of the presented strategy is verified through cosimulation experiments compared with the traditional three-loop PID method. The performance of the electrohydrostatic position actuation system, such as in nonovershoot regulation to step signal, stronger rejection capability to an external disturbance, higher frequency bandwidth and tracking accuracy to sinusoidal signal, and wide stability margin to parametric variation, is significantly improved.

In addition, the developed DSMO can achieve the finite time estimation instead of the bounded estimation, and its stability proof process is easier than the existing finite time observer. The designed reaching law can simultaneously acquire the desirable performance of fast reaching rate and chattering alleviation through the adaptive regulation of switch gain. The shape of the chattering band is fusiform, which is particularly distinct from several traditional reaching laws.

Conflicts of Interest

The authors declare no conflicts of interest regarding the publication of this article.

Acknowledgments

This work was supported by the National Natural Science Foundation of China (Grant no. 51505016) and Aeronautical Science Foundation of China (Grant no. 20152851020).

References

[1] J. Maré and J. Fu, "Review on signal-by-wire and power-by-wire actuation for more electric aircraft," *Chinese Journal of Aeronautics*, vol. 30, no. 3, pp. 857–870, 2017.

[2] S. L. Botten, C. R. Whitley, and A. D. King, "Flight control actuation technology for next-generation all-electric Aircraft," *Technology Review Journal*, pp. 55–68, 2000.

[3] F. Kou, "The control study of vehicle active suspension with Electro-Hydrostatic Actuator," *Applied Mechanics and Materials*, vol. 97-98, pp. 716–720, 2011.

[4] W. Sun, H. Gao, and B. Yao, "Adaptive robust vibration control of full-car active suspensions with electrohydraulic actuators," *IEEE Transactions on Control Systems Technology*, vol. 21, no. 6, pp. 2417–2422, 2013.

[5] J. Kovář, "Electro-hydraulic control of injection moulding machine for plastic," *Review of Scientific Instruments*, vol. 65, no. 11, pp. 3408–3414, 2011.

[6] S. Park, M. Park, and Y. Joung, "Practical Application Example of an Electro Hydrostatic Actuator(Development of 3000 ton Injection Molding Machine)," *Journal of The Korean Society for Fluid Power & Construction Equipments*, vol. 9, no. 3, pp. 56–66, 2012.

[7] M.-H. Chiang, C.-C. Chen, and C.-F. J. Kuo, "The high response and high efficiency velocity control of a hydraulic injection molding machine using a variable rotational speed electro-hydraulic pump-controlled system," *The International Journal of Advanced Manufacturing Technology*, vol. 43, no. 9-10, pp. 841–851, 2009.

[8] S. Alfayad, F. B. Ouezdou, F. Namoun, and G. Gheng, "High performance integrated electro-hydraulic actuator for robotics - Part I: Principle, prototype design and first experiments," *Sensors and Actuators A: Physical*, vol. 169, no. 1, pp. 115–123, 2011.

[9] S. Alfayad, F. B. Ouezdou, F. Namoun, and G. Gheng, "High performance Integrated Electro-Hydraulic Actuator for robotics. Part II: Theoretical modelling, simulation, control & comparison with real measurements," *Sensors and Actuators A: Physical*, vol. 169, no. 1, pp. 124–132, 2011.

[10] H. Kaminaga, H. Tanaka, and Y. Nakamura, "Mechanism and control of knee power augmenting device with back drivable electro-hydrostatic actuator," in *Proc. of 13th World Congress in Mechanism and Machine Science*, vol. A12, p. 534, 2011.

[11] G. Z. Zhou, Y. L. Fu, H. T. Qi, and et al., "Force based impedance control of electro-hydrostatic actuator," *Journal of Beijing University of Aeronautics & Astronautics*, vol. 43, no. 1, pp. 93–99, 2017.

[12] J. Li, Y. L. Fu, Z. L. Wang, and et al., "Research on fast response and high accuracy control of an airborne electro hydrostatic actuation system," in *Proceedings of the 2004 International Conference on Intelligent Mechatronics and Automation*, pp. 428–432, Chengdu, China, 2004.

[13] J. Zheng, S. Zhao, and S. Wei, "Application of self-tuning fuzzy PID controller for a SRM direct drive volume control hydraulic press," *Control Engineering Practice*, vol. 17, no. 12, pp. 1398–1404, 2009.

[14] M. A. El Sayed and S. Habibi, "Inner-loop control for electro-hydraulic (EHA) actuation systems," in *Proceedings of the 2009 ASME Dynamic Systems and Control Conference, DSCC2009*, pp. 1563–1570, USA, October 2009.

[15] G. Ren, M. Esfandiari, J. Song, and N. Sepehri, "Position Control of an Electrohydrostatic Actuator with Tolerance to Internal Leakage," *IEEE Transactions on Control Systems Technology*, vol. 24, no. 6, pp. 2224–2232, 2016.

[16] K. Kang, M. Pachter, C. H. Houpis, and S. Rasmussen, "Modeling and control of an electro-hydrostatic actuator," in *Proceedings of the IEEE 1995 National Aerospace and Electronics Conference. Part 2 (of 2)*, pp. 545–556, May 1995.

[17] S. H. Cho and R. Burton, "Position control of high performance hydrostatic actuation system using a simple adaptive control (SAC) method," *Mechatronics*, vol. 21, no. 1, pp. 109–115, 2011.

[18] H. Zhang, X. Liu, J. Wang, and H. R. Karimi, "Robust H ∞, sliding mode control with pole placement for a fluid power electrohydraulic actuator (EHA) system," *The International Journal of Advanced Manufacturing Technology*, 2014.

[19] Q. Zhang and B. Li, "Feedback linearization PID control for electro-hydrostatic actuator," in *Proceedings of the 2011 2nd International Conference on Artificial Intelligence, Management Science and Electronic Commerce, AIMSEC 2011*, pp. 358–361, China, August 2011.

[20] M. L. Ji, M. K. Han, S. H. Park, and et al., "A position control of electro-hydraulic actuator systems using the adaptive control scheme," in *Proceedings of the Asian Control Conference*, pp. 21–26, IEEE, 2009.

[21] K. K. Ahn, D. N. C. Nam, and M. Jin, "Adaptive backstepping control of an electrohydraulic actuator," *IEEE/ASME Transactions on Mechatronics*, vol. 99, pp. 1–9, 2013.

[22] H. Sun, T. Meinlschmidt, and H. Aschemann, "Passivity-based control of a hydrostatic transmission with unknown disturbances," in *Proceedings of the 2014 19th International Conference on Methods and Models in Automation and Robotics, MMAR 2014*, pp. 94–99, Poland, September 2014.

[23] J. Yao, Z. Jiao, and D. Ma, "Extended-state-observer-based output feedback nonlinear robust control of hydraulic systems with backstepping," *IEEE Transactions on Industrial Electronics*, vol. 61, no. 11, pp. 6285–6293, 2014.

[24] Q. Guo, Y. Zhang, B. G. Celler, and S. W. Su, "Backstepping Control of Electro-Hydraulic System Based on Extended-State-Observer with Plant Dynamics Largely Unknown," *IEEE Transactions on Industrial Electronics*, vol. 63, no. 11, pp. 6909–6920, 2016.

[25] S. Wang, R. Burton, and S. Habibi, "Sliding mode controller and filter applied to an electrohydraulic actuator system," *Journal of Dynamic Systems, Measurement, and Control*, vol. 133, no. 2, Article ID 024504, 2011.

[26] M. Perron, J. De Lafontaine, and Y. Desjardins, "Sliding-mode control of a servomotor-pump in a position control application," in *Proceedings of the Canadian Conference on Electrical and Computer Engineering*, pp. 1287–1291, Saskatoon, Canada, May 2005.

[27] S. Wang, S. Habibi, and R. Burton, "Sliding mode control for an electrohydraulic actuator system with discontinuous non-linear friction," *Proceedings of the Institution of Mechanical Engineers, Part I: Journal of Systems and Control Engineering*, vol. 222, no. 8, pp. 799–815, 2008.

[28] H. Sun and H. Aschemann, "Sliding-mode control of a hydrostatic drive train with uncertain actuator dynamics," in *Proceedings of the 2013 12th European Control Conference, ECC 2013*, pp. 3216–3221, che, July 2013.

[29] J. M. Lee, S. H. Park, and J. S. Kim, "Design and experimental evaluation of a robust position controller for an electrohydrostatic actuator using adaptive antiwindup sliding mode scheme," *The Scientific World Journal*, vol. 2013, Article ID 590708, 2013.

[30] Z. Q. Shi, Z. Tang, and C. Pei, "Sliding mode control for electrohydrostatic actuator," *Computer Measurement & Control*, 2014.

[31] H.-M. Chen, J.-C. Renn, and J.-P. Su, "Sliding mode control with varying boundary layers for an electro-hydraulic position servo system," *The International Journal of Advanced Manufacturing Technology*, vol. 26, no. 1-2, pp. 117–123, 2005.

[32] A. Levant, "Higher-order sliding modes, differentiation and output-feedback control," *International Journal of Control*, vol. 76, no. 9-10, pp. 924–941, 2003.

[33] F. Plestan, Y. Shtessel, V. Brégeault, and A. Poznyak, "New methodologies for adaptive sliding mode control," *International Journal of Control*, vol. 83, no. 9, pp. 1907–1919, 2010.

[34] Y. L. Fu, Z. F. Li, and J. Xue, *A kind of Permanentmagnet axial piston integrated electro-hydraulic pump with speedfeedback*, China, ZL201320520163.3, 2014.

[35] R. R. Yang, Y. L. Fu, and Y. Wang, "Free-chattering fractional order sliding mode control of integrated electro-hydraulic servo pump," *Journal of Beijing University of Aeronautics Astronautics*, vol. 42, no. 8, pp. 1649–1658, 2016.

[36] P. Ponomarev, M. Polikarpova, O. Heinikainen, and J. Pyrhönen, "Design of integrated electro-hydraulic power unit for hybrid mobile working machines," in *Proceedings of the 2011 14th European Conference on Power Electronics and Applications, EPE 2011*, September 2011.

[37] H. Zhang and J. Wang, "Adaptive Sliding-Mode Observer Design for a Selective Catalytic Reduction System of Ground-Vehicle Diesel Engines," *IEEE/ASME Transactions on Mechatronics*, vol. 21, no. 4, pp. 2027–2038, 2016.

[38] W.-H. Chen, "Nonlinear disturbance observer-enhanced dynamic inversion control of missiles," *Journal of Guidance, Control, and Dynamics*, vol. 26, no. 1, pp. 161–166, 2003.

[39] Q. Zheng, L. Q. Gao, and Z. Gao, "On stability analysis of active disturbance rejection control for nonlinear time-varying plants with unknown dynamics," in *Proceedings of the 46th IEEE Conference on Decision and Control (CDC '07)*, pp. 3501–3506, New Orleans, La, USA, December 2007.

[40] J. Qian, A. Xiong, and W. Ma, "Extended State Observer-Based Sliding Mode Control with New Reaching Law for PMSM Speed Control," *Mathematical Problems in Engineering*, vol. 2016, Article ID 6058981, 2016.